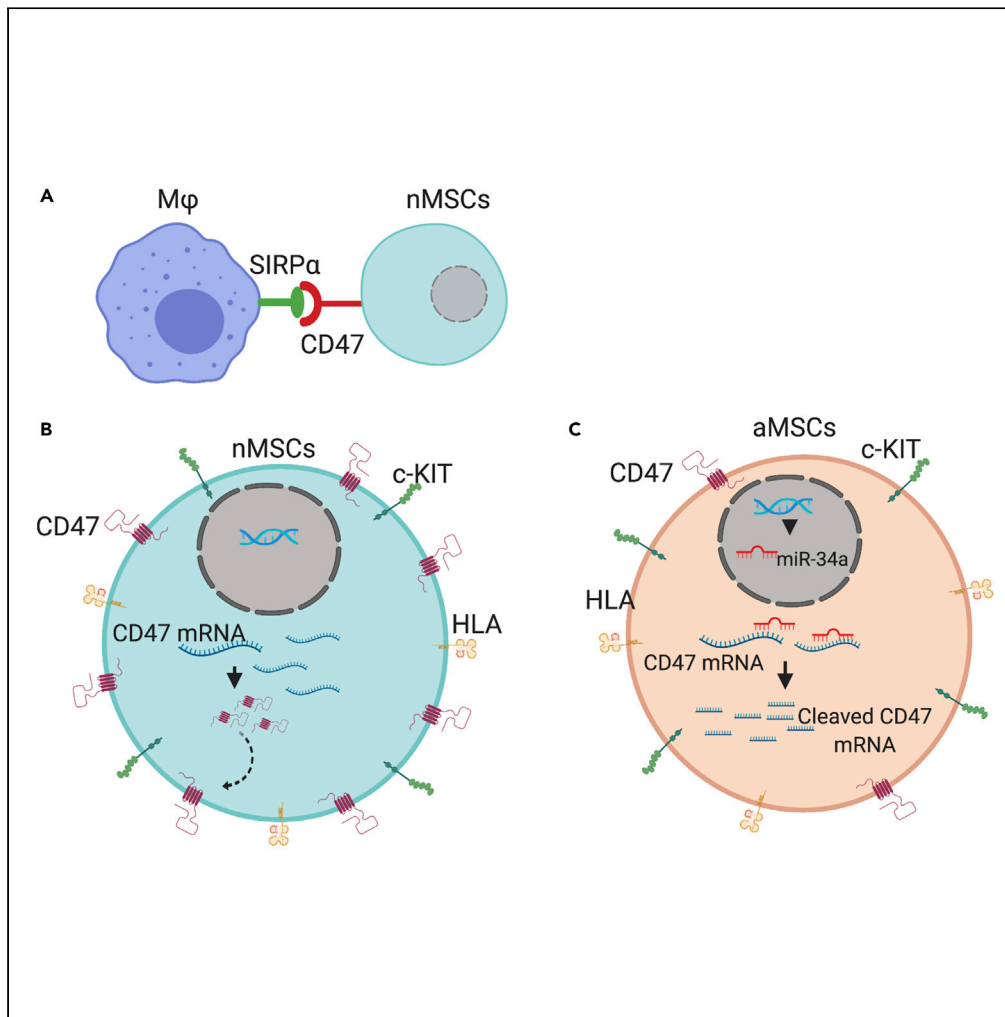## Article

Comparative efficacy and mechanism of action of cardiac progenitor cells after cardiac injury

Muthukumar
Gunasekaran,
Rachana Mishra,
Progyaparamita
Saha, ..., Joshua
M. Hare, Sudhish
Sharma, Sunjay
Kaushal

susharma@luriechildrens.org
(S.S.)
skaushal@luriechildrens.org
(S.K.)

Highlights

nMSCs are the most
potent cell type yet to
recover injured
myocardium

CD47 assisted immune
evasion increases nMSCs'
retention

miR34a-5p regulate CD47
and the composition of
nMSCs secretome

iScience

Article

Comparative efficacy and mechanism of action of cardiac progenitor cells after cardiac injury

Muthukumar Gunasekaran,[1,8] Rachana Mishra,[1,8] Progyaparamita Saha,[1] David Morales,[1] Wen-Chih Cheng,[2] Arun R. Jayaraman,[3] Jessica R. Hoffman,[3] Lauran Davidson,[1] Ling Chen,[1] Aakash M. Shah,[1] Gregory Bittle,[1] Xuebin Fu,[1] Antariksh Tulshyan,[1] Mohamed Abdullah,[1,4] Tami Kingsbury,[5] Curt Civin,[2] Peixin Yang,[1] Michael E. Davis,[3] Roberto Bolli,[6] Joshua M. Hare,[7] Sudhish Sharma,[1,*] and Sunjay Kaushal[1,9,*]

SUMMARY

Successful cell therapy requires cells to resist the hostile ischemic myocardium, be retained to continue secreting cardioprotective growth factors/exosomes, and resist immunological host responses. Clinically relevant stem/progenitor cells in a rodent model of acute myocardial infarction (MI) demonstrated that neonatal cardiac mesenchymal stromal cells (nMSCs) provide the most robust cardiac functional recovery. Transplanted nMSCs significantly increased the number of tissue reparative macrophages and regulatory T-cells and decreased monocyte-derived inflammatory macrophages and neutrophils in the host myocardium. mRNA microarray and single-cell analyses combined with targeted depletion studies established CD47 in nMSCs as a key molecule responsible for cell retention in the myocardium through an antiphagocytic mechanism regulated by miR34a-5p. Gain and loss-of-function studies demonstrated that miR34a-5p also regulated the production of exosomes and cardioprotective paracrine factors in the nMSC secretome. In conclusion, miR34a-5p and CD47 play an important role in determining the composition of nMSCs' secretome and immune evasion, respectively.

INTRODUCTION

As a potential therapeutic agent, cardiac stem cells adapt to the microenvironment of the infarcted myocardium and secrete specific growth factors, chemokines, cytokines, and miRNA-enriched exosomes to improve cardiac function and prevent adverse cardiac remodeling after myocardial infarction (MI) (Sharma et al., 2017). To optimize stem cell efficacy, it is critical to prolong stem cell retention in the infarcted myocardium and to maximize the potency of the stem cell secretome, which is the major mediator of stem cell function. Since the chronological age of the stem cells is a major determinant of secretome potency and all clinical trials conducted so far have used stem cells generated from adults (aged >18 years), clinical trials using cardiac stem cells have had mixed and inconsistent results in adult patients with MI (Telukuntla et al., 2013). Additionally, a recent report attributing the functional benefit of cardiac stem cell therapy to an acute, inflammation–based wound-healing response that occurs even when dead cells are injected into the infarcted myocardium fails to explain the positive remodeling changes in the infarcted myocardium that are seen after intravenous administration of stem cells (Vagnozzi et al., 2020). These results underscore the importance of more carefully examining the mechanistic basis of cell therapy.

Immediately following MI, neutrophils (CD11b/c[+]/RP-1^{+}) are recruited to the site of injury to clear necrotic tissue and debris via their proteases. Neutrophils activate a cascade that promotes macrophage polarization from proinflammatory M1 (CD68^{+}/CCR2^{+}) to anti-inflammatory M2 (CD206^{+}/CD163^{+}) macrophages that secrete anti-inflammatory cytokines. Recent studies have found that increased macrophage subsets or regulatory T-cells can restore cardiac function and alleviate negative cardiac remodeling in injured myocardium (Frangogiannis, 2012; Nahrendorf et al., 2010) (Shiraishi et al., 2016). Studies with systemic depletion of macrophages or regulatory T cell (CD4^{+}/FoxP3^{+}/CD25^{+}) subpopulations, paired with adoptive transfer of each subpopulation, suggest that adaptive immunity also has an important function in regulating myocardial repair (Rieckmann et al., 2019). A recent comprehensive analysis of the cardiac stem cell secretome, comprising independently secreted cytokines and exosomes, has identified key molecular

[1]Departments of Surgery and Pediatrics, Ann and Robert H. Lurie Children's Hospital of Chicago, Feinberg School of Medicine, Northwestern University, 225 E. Chicago Avenue, Chicago, IL 60611, USA

[2]Center for Stem Cell Biology and Regenerative Medicine, Department of Pediatrics, University of Maryland School of Medicine, Baltimore, MD 21201, USA

[3]Wallace H. Coulter Department of Biomedical Engineering, Emory University and Georgia Institute of Technology, 1760 Haygood Drive, W200, Atlanta, GA 30322, USA

[4]Department of Cardiothoracic Surgery, Cairo University, Cairo 11553, Egypt

[5]Center for Stem Cell Biology and Regenerative Medicine, Department of Physiology, University of Maryland School of Medicine, Baltimore, MD 21201, USA

[6]Institute of Molecular Cardiology, University of Louisville, Louisville, KY 40202, USA

[7]University of Miami, Miller School of Medicine, Miami, FL, USA

[8]These authors contributed equally

[9]Lead contact

*Correspondence:
susharma@luriechildrens.org
(S.S.),
skaushal@luriechildrens.org
(S.K.)

https://doi.org/10.1016/j.isci.2022.104656

pathways that potentially control neutrophil activation (short-lived to prevent collateral damage to the myocardium), M2 polarization of macrophages, and immune rejection, which together may optimize positive remolding of the infarcted myocardium (Duran et al., 2013; Segers and Lee, 2008; Vasandan et al., 2016; Wehman and Kaushal, 2015). We investigated these pathways in this study.

Thus far, in more than 200 clinical trials to treat MI, multiple stem cell types sourced from various adult tissues have been evaluated with limited success. A possible reason for the inconclusive results is the uncertainty regarding the mechanism of action. Accordingly, the goal of this study was to elucidate the underlying mechanisms by which cardiac stem cells act to restore cardiac function in the infarcted myocardium. Using single-cell RNA sequencing, and other gain- and loss-of-function approaches, we investigated the efficacy of various clinically relevant human stem/progenitor cells currently being tested in clinical practice. Specifically, we addressed the following questions: (1) Which stem cell type most effectively repairs the injured myocardium? (2) What is the effect of transplanted stem cells on immune cells? (3) How do transplanted stem cells evade phagocytosis, which allows longer retention? (4) What is the overall mechanism for immune evasion by the transplanted cells? (5) Can a master regulator define the composition of the transplanted cell secretome? Considering the complex composition of the cellular secretome, we sought to characterize the diverse phenomena targeted by transplanted cells in the host myocardium and to dissect the molecular signaling pathways responsible for cardiac repair.

RESULTS

Comparative efficacy of stem and progenitor cells in a rodent Foxn1 mutant MI model

To determine the most potent progenitor cell type in a relevant, preclinical Foxn1 mutant (nude) rodent MI model, we examined cardiac function after cell injection using well-studied progenitor cell types in a head-to-head, blinded, randomized study. Following standard characterization of each progenitor cell type (Figures S1A and S1B), nMSCs, adult mesenchymal stromal cells (aMSCs), adult cardiosphere-derived cells (aCDCs), umbilical cord blood cells (UCBCs), BM-MSCs, or the placebo control containing cell-free Iscove's Modified Dulbecco Medium (IMDM) were injected into the MI border zone in immunodeficient RNU rats in order to the determine the effects of therapy independent of the confounding influences of the immune system. Importantly, all groups had similar left ventricular ejection fractions and fractional shortening at 24 h post-MI, indicating that the size of the MI was similar in all groups (Figures 1A and 1B). Consistent with previous reports, 4 weeks after the MI and injections, left ventricular function had improved significantly in the groups injected with nMSCs, aMSCs, aCDCs, UCBCs, or BM-MSCs compared with placebo-injected controls. More importantly, nMSCs significantly outperformed all other progenitor cell types in improving the function of the injured myocardium. Histological analysis of the explanted heart tissue was performed 4 weeks post-MI by Masson trichrome staining, and infarct size was determined by measuring the area of fibrosis (blue) relative to the total stained myocardial area (blue and pink). Regions of red staining (viable tissue) within predominantly blue-stained regions (fibrous tissue) were typically seen in all hearts. Examination of heart sections revealed a significant decrease in fibrosis in CDCs, BM-MSCs and aMSCs treatment groups, however the most significant decrease in fibrosis was identified in nMSCs treatment group (Figures 1C and 1D).

To profile post-MI myocardial inflammation, histological foci of acute inflammation were observed within the infarct border zone at 1-week post-MI. After 1 week, there was a significant increase in activated CD68^{+} inflammatory macrophages within the areas of aMSC injection, but they were significantly diminished in the areas injected with nMSCs. Staining of myocardial sections also demonstrated that nMSC injection stimulated higher levels of CD163^{+} anti-inflammatory macrophages (Figures S2A–S2C).

To further evaluate the immune modulation affected by nMSCs, we performed a randomized, blinded study in an immunocompetent rat model of MI in which we injected nMSCs, aMSCs, or placebo (IMDM). Before injection, we assessed the angiogenic potential of selected stem cell types by performing wound-healing assays on human mammary epithelial cells. The wound area was significantly reduced in the presence of nMSCs compared with placebo (Figures S3A and S2B). Importantly, the injected nMSCs significantly outperformed aMSCs, BM-MSCs, and placebo in improving ventricular function at 4 weeks in the rat MI model (Figures 1E and 1F). We have previously identified HSF1 as a master regulator of the secretome of stem cells (Sharma et al., 2017), responsible for the presence of cardioprotective factors therein. Immunoblot and RNA expression analysis showed significantly higher expression of HSF1 in nMSCs as compared to any other cell type showing significant improvement in cardiac function
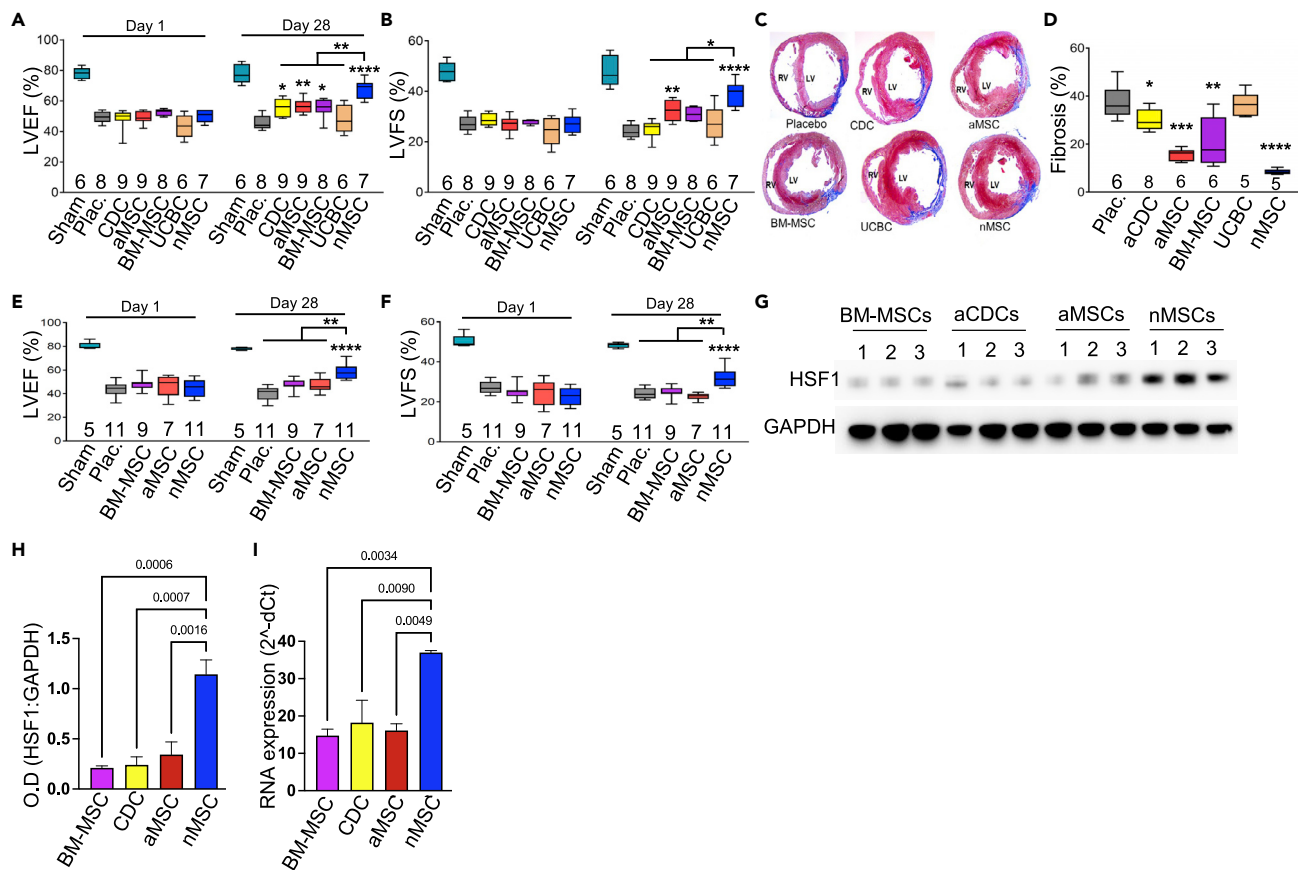
Figure 1. Cardiac functional outcomes following stem cell transplantation in the MI model

(A and B) Left ventricular ejection fraction (LVEF) (A) and fractional shortening (LVFS) (B) derived from echocardiography are shown for post-operative day (POD) one and POD 28 with different cell therapies (N = 6–9) in RNU rat MI model. At POD 1, no significant difference was observed.

(C and D) (C) At POD 28, Masson trichrome staining of hearts sections after nMSCs, or placebo control or stem cell types; quantitative assessment is shown in (D) (N = 5–8).

(E and F) LVEF (E) and LVFS (F) derived from echocardiography are shown for POD one and POD 28 for treatment with nMSCs compared with BM-MSCs, aMSCs, and placebo (N = 5–11) in immuno-component Brown-Norway rat MI model.

(G–I) Immunoblot analysis (G and H) and real-time PCR analysis (I) showing the expression of HSF1 in BM-MSC, aCDCs, aMSC and nMSCs.

Data were analyzed by One-way ANOVA using Prism GraphPad[Tm] software and represented as mean $\pm$ SEM (*p < 0.05, **p < 0.01, ***p < 0.001 and ****p < 0.0001).

(Figures 1G–1I). Taken together, our results support the idea that HSF1 represents a candidate protective mechanism common to all the cell types tested, but highly expressed in nMSCs.

Immune cell analysis following MSC injection in the Brown Norway rat MI model

Immunohistochemical analysis of heart tissues after 2 days, showed significant up-regulation of activated inflammatory CD68^{+}CCR2^{+} or CD68^{+}CX3CR1^{+} macrophage subsets in hearts injected with aMSCs or the placebo control (IMDM) (Figures 2A, 2B, 2D, and 2E). In contrast, hearts injected with nMSCs showed significant decreases in these macrophage subsets (Figures 2A, 2B, 2D, and 2E). In addition, the injected nMSCs significantly increased anti-inflammatory CD68^{+}CD163^{+} macrophage levels compared with the other study groups (Figures 2C and 2F).

Using single-cell suspensions from freshly-obtained, leukocyte-enriched fractions of whole hearts at 5 days post-MI, we analyzed macrophages, neutrophils, T cells, T regulatory cells (Tregs), and dendritic cells by flow cytometry. Compared with injection of placebo, we found that the injected nMSCs significantly decreased inflammatory CD68^{+}/CD45^{+} macrophage levels and CD11b/c^{+}/R1^{+} neutrophil levels while significantly increasing CD4^{+}/CD25^{+}/FoxP3^{+} Treg levels (Figures 2G and 2H). All injected groups had similar levels of total T cells (CD3^{+}), cytotoxic T cells (CD3^{+}/CD8^{+}), and dendritic cells (CD45^{+}/CD11c^{+}/MHC-CII) (Figures S4A–S4G).
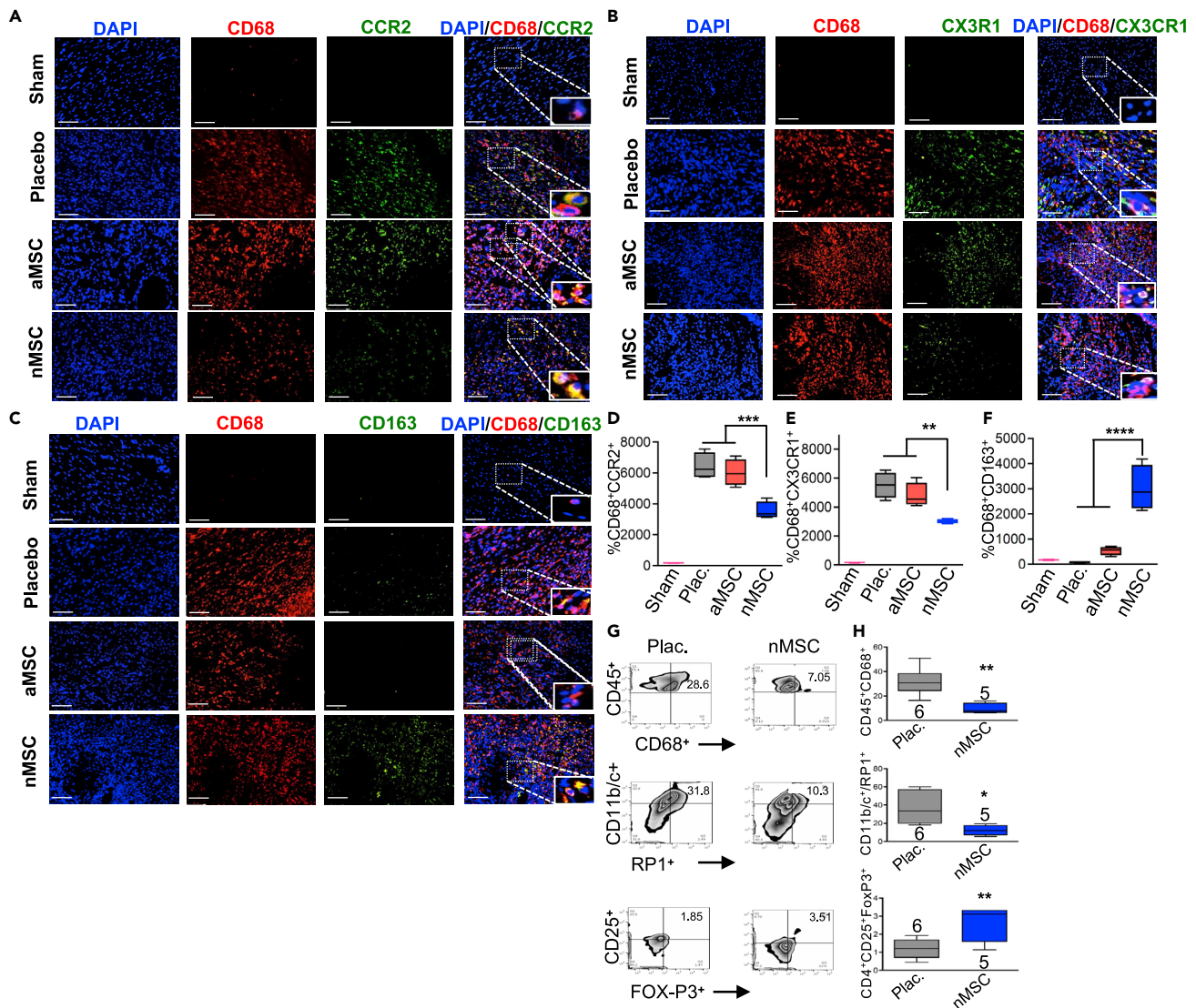
Figure 2. Immune cell analysis following MSC injection in the rat MI model

(A–C) Representative images of Day 2 heart tissues showing inflammatory CD68+CCR2+ (A) or CD68+CX3C1+ (B) macrophages and anti-inflammatory CD68 + 163+ macrophages (C) in the rat myocardium after injection of aMSCs, nMSCs, placebo, or sham controls (scale bars = 75 μm).

(D–H) Quantitative assessment of CD68+CCR2+ cells (D), CD68+CX3C1+ cells (E), and CD68 + 163+ cells (F) in MI hearts after nMSC injection, as compared with placebo controls (N = 4–5). Phenotypic characterization of macrophages (CD45+ CD68+), neutrophils (CD11b/c+/R1+), and regulatory T cells (Tregs; CD4+CD25+FoxP3+) in rat hearts following nMSC transplantation compared with placebo injection (G) (N = 5–6). Representative histograms show flow cytometry analyses of macrophages, neutrophils, and Tregs (H).

Data were analyzed by One-way ANOVA using Prism GraphPad[Tm] software and represented as mean ± SEM (*p < 0.05, **p < 0.01, ***p < 0.001 and ****p < 0.0001).

To further assess cardiac function in an immunocompetent rat MI model, we injected human cardiac-derived nMSCs and their adult counterparts, aMSCs, in the infarcted myocardium with and without immunosuppressive treatment involving cyclosporine A (CSA). Compared with injection of aMSCs or the placebo control (IMDM), injection of nMSCs produced significant improvement in cardiac function (Figures S5A–S5D). Importantly, injection of aMSCs with CSA treatment significantly improved cardiac function when compared with injection of aMSCs alone at 4 weeks post-MI (Figures S5A and S5B), suggesting that dampening the immune response is critical for optimizing the cardiac reparative potential of aMSCs. Strikingly, injected nMSCs significantly improved cardiac function independent of CSA treatment (S5c,d), suggesting active immunomodulation. During the post-treatment period, injected nMSCs significantly dampened levels of the inflammatory cytokines interleukin (IL)-4 and IL-12 but increased levels of anti-inflammatory

IL-10 in plasma collected on post-injection days 2 and 7 in the same MI rat model (Figures S6A–S6C), consistent with immunomodulatory action.

nMSCs evade phagocytosis *in vivo* and *in vitro*

Studies from our laboratory and others have demonstrated that injected progenitor cells fail to differentiate into mature cardiomyocytes in the MI model; thus, an alternative mechanism must be responsible for functional recovery (Sharma et al., 2017). Through a deep proteomic analysis, we previously determined that the complete secretome, comprised of independently secreted cytokines and exosomes, is the progenitor cell compartment with the ability to fully functionally repair the myocardium post-MI (Sharma et al., 2017). Beyond the immune modulation mechanism defined above, we additionally explored three potential mechanisms by which nMSCs may promote functional recovery of the injured myocardium: cell retention; independently secreted cytokines; and secreted exosomes. To explore these molecular pathways, we performed a comparative analysis of nMSCs and aMSCs.

First, to determine if nMSCs increase cell retention by inhibiting phagocytosis, we performed *in vitro* and *in vivo* phagocytosis assays with green fluorescent protein (GFP)-labeled nMSCs (nMSC^{GFP+}) and aMSCs (aMSC^{GFP+}) using macrophages derived from THP-1 cells as the phagocytic cells (Figures 3A and 3B). aMSCs^{GFP+} significantly increased phagocytosis by M1 PKH26 macrophages in a co-culture experiment. In contrast, nMSCs^{GFP+} inhibited phagocytosis by M1 PKH26 macrophages, enabling nMSCs^{GFP+} proliferation (Figures 3C and 3D). Similarly, injection of nMSCs^{GFP+} in the immunocompetent Brown Norway rat MI model resulted in minimal phagocytosis and thus significantly increased cell retention. In contrast, injection of aMSCs^{GFP+} resulted in increased phagocytosis and minimal cell retention (Figures 3E and 3F). These results are consistent with current models of cancer cell proliferation and migration in which tumor progression is promoted by an antiphagocytic mechanism that dampens the inflammatory response and facilitates cancer cell immune evasion (Alvey and Discher, 2017; Métayer et al., 2017).

RNA sequencing of nMSCs and aMSCs

To further determine the cellular mechanism underlying the antiphagocytic actions of nMSCs, we performed bulk RNA sequencing (Illumina TreSeq with a minimum of 25 million paired-end reads per sample) to identify mRNAs that are differentially expressed in nMSCs and aMSCs. Among the top hits affecting immunomodulation, CD47 mRNA expression was 1.7-fold higher in nMSCs than in aMSCs (p = 0.015) (Figures 4A–4C and Table S1). This was consistent with our previous deep quantitative comparative proteomic analysis, which revealed CD47 to be among the eight most highly represented proteins in nMSCs compared with aMSCs (Sharma et al., 2017). CD47 is a key antiphagocytic molecule and is upregulated by a variety of cancers, rendering malignant cells resistant to phagocytosis stimulated by the immune surveillance machinery (Chao et al., 2012; Jaiswal et al., 2009; Kamerkar et al., 2017; Majeti et al., 2009; Willingham et al., 2012; Zhang et al., 2018).

To further resolve the differences between nMSCs and aMSCs, cells were sequenced with 10x Genomics single-cell technology and analyzed for transcriptional heterogeneity across cell subpopulations (Figure 4D). nMSCs and aMSCs were clustered into four groups using the Leiden community detection algorithm (Figure 4E). Gene expression analysis indicated that the first 2 clusters had high expression of CD47, platelet-derived growth factor subunit A (PDGF-A), hepatocyte growth factor (HGF), insulin-like growth factor 1 (IGF-1), fibroblast growth factor 2 (FGF-2), vascular endothelial growth factor A (VEGF-A), and stromal cell-derived factor (SDF1/CXCL12) (Figure 4F), with nMSCs especially overrepresented in Cluster 2, whereas aMSCs were overrepresented in cluster 3 (Figure 4G). Cluster three had especially low expression of CD47 and SDF1/CXCL12 compared with the other 3 clusters. Notably, Cluster four makes up a significantly smaller proportion of cells (3%) than the other cell clusters (Cluster 1: 39%; Cluster 2: 29%; Cluster 3: 29%). Upregulated genes in the nMSC-enriched Cluster two were associated with the cell cycle and proliferation, whereas those in the aMSC-enriched Cluster three correlated with leukocyte migration and cell death (Figures 4H and 4I). Similar analyses of Clusters one and four indicate that the former is upregulated in genes associated with integrin interactions, supramolecular fiber organization, and the wound-healing response, whereas the latter is upregulated in genes involved in ribosomal activity and the VEGF-A–VEGF receptor two signaling pathway (Figure S7A). In addition, fibronectin gene expression, which was previously implicated as an essential cardiac repair protein in nMSC-based therapies (Konstandin et al., 2013), is upregulated in Cluster one cells (Figure S7B). These results indicate that the differing functional responses of aMSCs and nMSCs may be attributed to a few subpopulations of cells. Specifically, increased
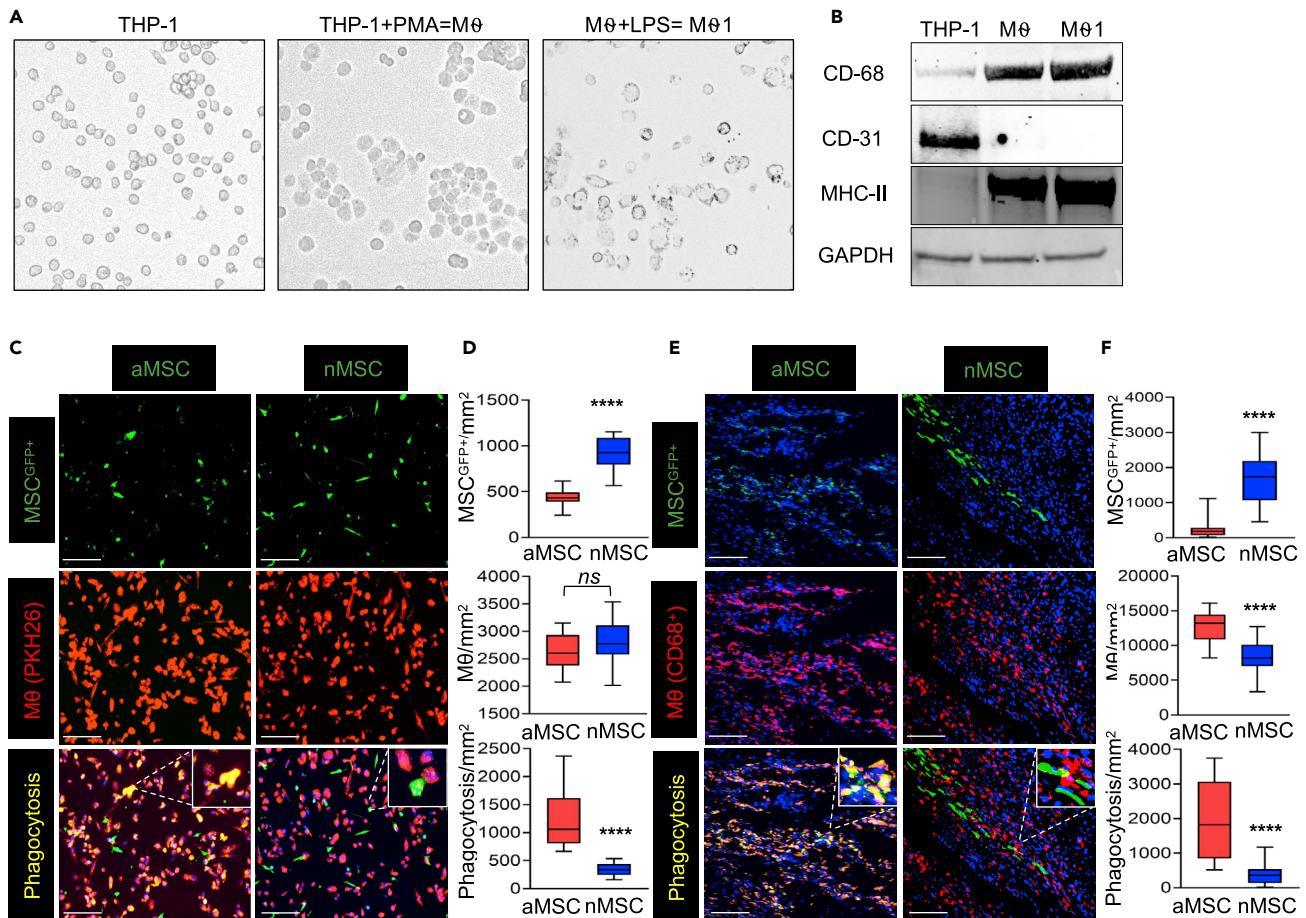
Figure 3. Cardiac nMSCs evade phagocytosis

(A) Representative micrographs of human monocytes (THP-1) differentiated into macrophages (Mφs).

(B) Immunoblot results show expression of the monocyte marker CD31 in monocytes and its reduction following Phorbol 12-myristate 13-acetate (PMA; differentiation) and LPS (activation) treatment. In contrast, the Mφ phenotypic marker CD68 and MHC-II were observed only with PMA and lipopolysaccharide (LPS) treatment. Glyceraldehyde 3-phosphate dehydrogenase (GAPDH) served as a loading control.

(C) Representative images showing Mφ-mediated phagocytosis of nMSCs^{GFP+} or aMSCs^{GFP+} after 24 h in coculture. Scale bars = 75 μm.

(D) Quantification of nMSCs^{GFP+} or aMSCs^{GFP+} (cell retention, green) phagocytosis by Mφs (PKH26, red) after 24 h.

(E) Representative images following injection of nMSCs^{GFP+} or aMSCs^{GFP+}. The nMSCs are more proliferative, have reduced CD68 expressing cells, and reduced phagocytosis compared with aMSCs. (scale bars = 75 μm).

(F) Quantification of nMSC^{GFP+} retention and CD68$^+$ phagocytic cells compared with aMSCs^{GFP+} following injection in MI rats (N = 4).

Data were analyzed by Prism GraphPad^{Tm} software by nonparametric Mann Whitney test and represented as mean ± SEM (*p < 0.05, **p < 0.01, ***p < 0.001 and ****p < 0.0001).

phagocytosis associated with aMSCs may be attributed to the relatively high abundance of Cluster three cells in the population, whereas the increased proliferative and adhesive properties of nMSCs may be attributed to the higher abundance of Cluster one and two cells.

CD47 expression on nMSCs inhibits phagocytosis

To determine if the elevated CD47 expression in nMSCs might be responsible for preventing their phagocytosis, we evaluated CD47 expression in three biological replicates (from three patients) of nMSCs and aMSCs by immunoblot and observed significantly higher CD47 expression in nMSCs (Figures 5A and 5B). Comparative RNA expression analysis also showed significantly higher expression of CD47 in nMSCs as compared to any other cell type showing significant improvement in cardiac function (Figure 5C). To further demonstrate that CD47 mediates inhibition of nMSC phagocytosis, we performed *in vitro* and *in vivo* phagocytosis assays by blocking CD47 in nMSCs using a specific antibody to CD47 (α-CD47) or its isotypic control (Alvey and Discher, 2017; Chao et al., 2012; Goto et al., 2014). In co-culture with M1 PKH26
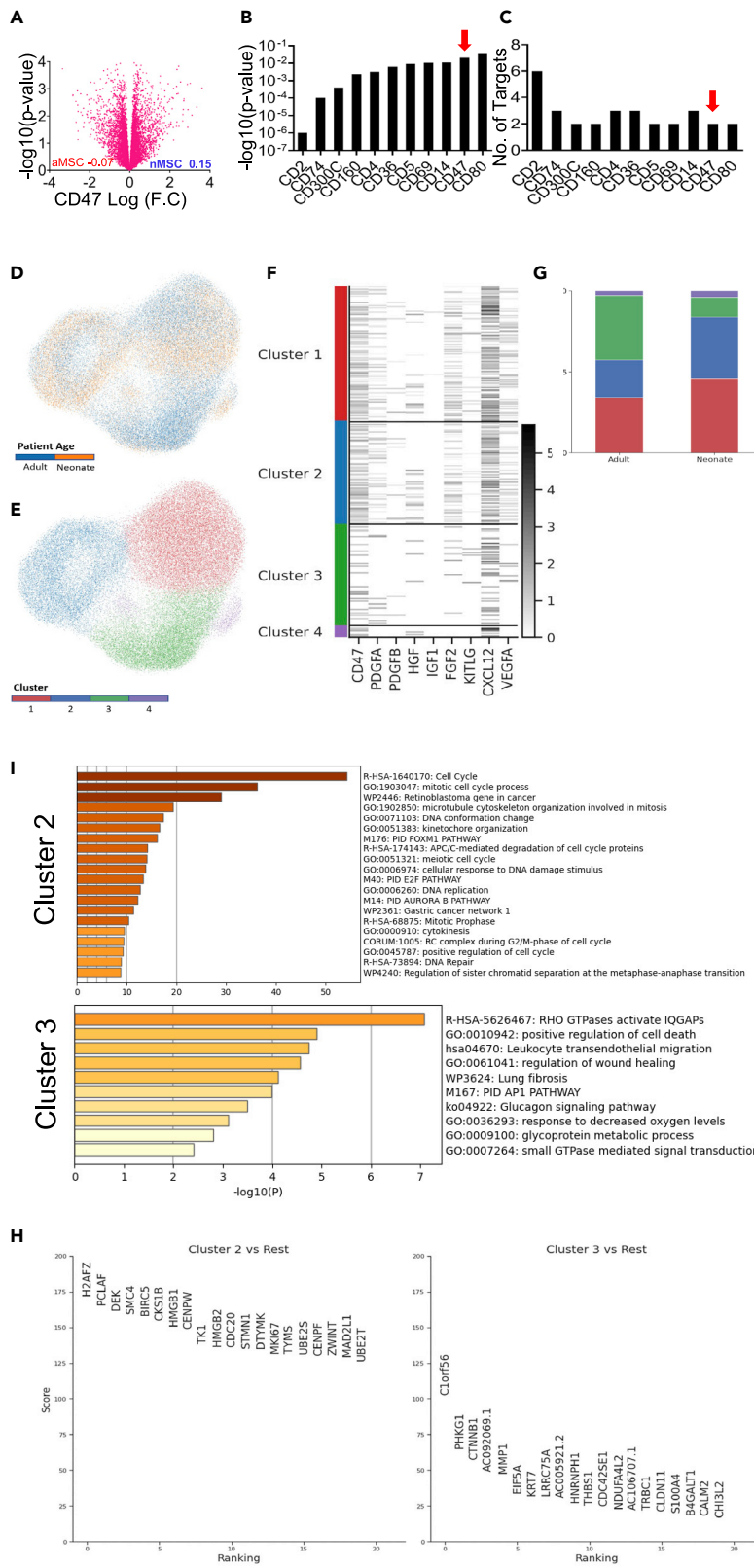
Figure 4. RNA sequencing of nMSCs and aMSCs

(A) Graphical representations of mRNA sequencing data. The mRNAs are ranked in a volcano plot according to their statistical (*p* value) significance (-log *P*; y axis) and the ratio of their relative abundance ratio (log$_2$-fold change; x axis) in nMSCs (blue) and aMSCs (red).

(B and C) Histogram representation of genes with significantly increased mRNA (B) and their targets (C).

(D) Uniform Manifold Approximation and Projection visualization of single-cell data collected from nMSCs (orange) and aMSCs (blue).

(E) Results of Leiden clustering at a resolution of 0.5.

(F) Heatmap of gene expression for selected genes within each cluster.

(G) The percentage of cells from either adult or neonate patient age groups in each cluster. Neonate cells are especially overrepresented in Cluster 2, whereas adult cells are overrepresented in Cluster 3.

(H) The top 20 upregulated genes, as determined by Scanpy, for Clusters two and 3.

(I) Metascape heatmap of GO terms obtained from the top 100 upregulated genes for Clusters two and 3. Upregulated genes in Cluster two correlate with cell cycle and proliferative activity, whereas upregulated genes in Cluster three correlate with increased leukocyte migration and cell death.

macrophages, nMSCs$^{\alpha-CD47}$ showed significantly increased phagocytosis compared with nMSCs$^{\alpha-isotype}$ (Figures 5D and 5E). Similarly, phagocytosis was significantly increased in rats injected with nMSCs$^{\alpha-CD47}$ compared with nMSCs$^{\alpha-isotype}$ (Figures 5F and 5G). Compared with nMSCs$^{\alpha-isotype}$ or IMDM controls, injection of nMSCs$^{\alpha-CD47}$ significantly diminished cardiac functional recovery, as assessed by echocardiography at 28 days (Figures 5H and 5I). Similarly, compared with scrambled siRNA or placebo IMDM treatments (Figures 5J and 5K), treatment of nMSCs with CD47 siRNA resulted in significantly decreased cardiac functional recovery. CD47 knockdown in nMSCs by siRNA was validated by immunoblot (Figure S8).

MicroRNA-34a-regulates CD47 and exosome secretion in nMSCs

To gain insights into regulation of CD47 and total secretome production, including independently secreted cytokines and exosomes, we examined the differential expression of microRNAs (miRNAs) in nMSCs and aMSCs by microarray analysis using the µParaflo Microfluidic Biochip and human arrays 2555. Principal component analysis of the data showed: a) segregation of nMSCs and aMSCs into two distinct groups, suggesting a direct role of aging on the miRNA composition of these cells; and b) remarkable similarities among biological replicates of nMSCs but profound variance among aMSCs (Figures 6A and 6B). Among the top 15 miRNAs with significantly differential expression (>2-fold), we identified high expression of four miRNAs in aMSCs (Figures 6A–6C). Among these, miR-34a stood out as being highly expressed in aMSCs compared with nMSCs (2.17-fold higher; p = 7.28 E-04). Interestingly, target scan analysis of miR-34a identified many target genes including those related to various cardioprotective paracrine factors, exosome production, and CD47 (Figures 6A–6C). This finding was verified by qRT-PCR in six different biological replicates (p > 0.01) (Figure 6D). In contrast, the expression levels of miR-34b and miR-34c were not statistically different between nMSCs and aMSCs (Figures S9A and S9B). Comparative RNA expression analysis also showed significantly lower expression of miR34a in nMSCs as compared to BM-MSC, CDC and aMSC (Figure 6E).

As miR-34a controls many proapoptotic processes during advancing chronological aging (Xu et al., 2012), we next examined the impact of miR-34a on the cellular properties of MSCs by performing loss- and gain-of-function experiments. Using lentiviral transduction, miR-34a was knocked down in aMSCs with the miR-34a sponge method and overexpressed in nMSCs with a miR-34a–expressing vector; an empty vector (EV) was used as a transduction control in all experiments. RT-PCR was used to confirm miR-34a knockdown in aMSCs and its overexpression in nMSCs (Figures S9C and S9D). We found that miR-34a overexpression in nMSCs significantly reduced their rate of cellular proliferation by increasing levels of the cell cycle inhibitors p16 and p21 and decreasing expression of the stem cell markers NANOG, KLF4, and SOX2 (Figures 6H, 6K, 6L, and S10). In contrast, knockdown of miR-34a in aMSCs significantly enhanced their rate of cellular proliferation and decreased levels of p16 and p21 (Figures 6G, 6I, and 6J).

To evaluate whether miR-34a regulates CD47, we examined the effects of miR-34a overexpression versus empty vehicle in nMSCs (nMSCs$^{miR-34A-OE}$). Immunoblot analysis revealed that miR-34a overexpression significantly reduced CD47 expression compared with nMSCs transfected with the empty vector (nMSCs^{EV}) (Figure 6M). In the MI model, injected nMSCs$^{miR-34A-OE}$ significantly reduced cardiac functional recovery at 28 days when compared with nMSCs^{EV} or nMSCs (Figures 6N and 6O). Similarly, injected aMSCs$^{miR-34a-kD}$ significantly improved cardiac function, when compared with injection of aMSCs or
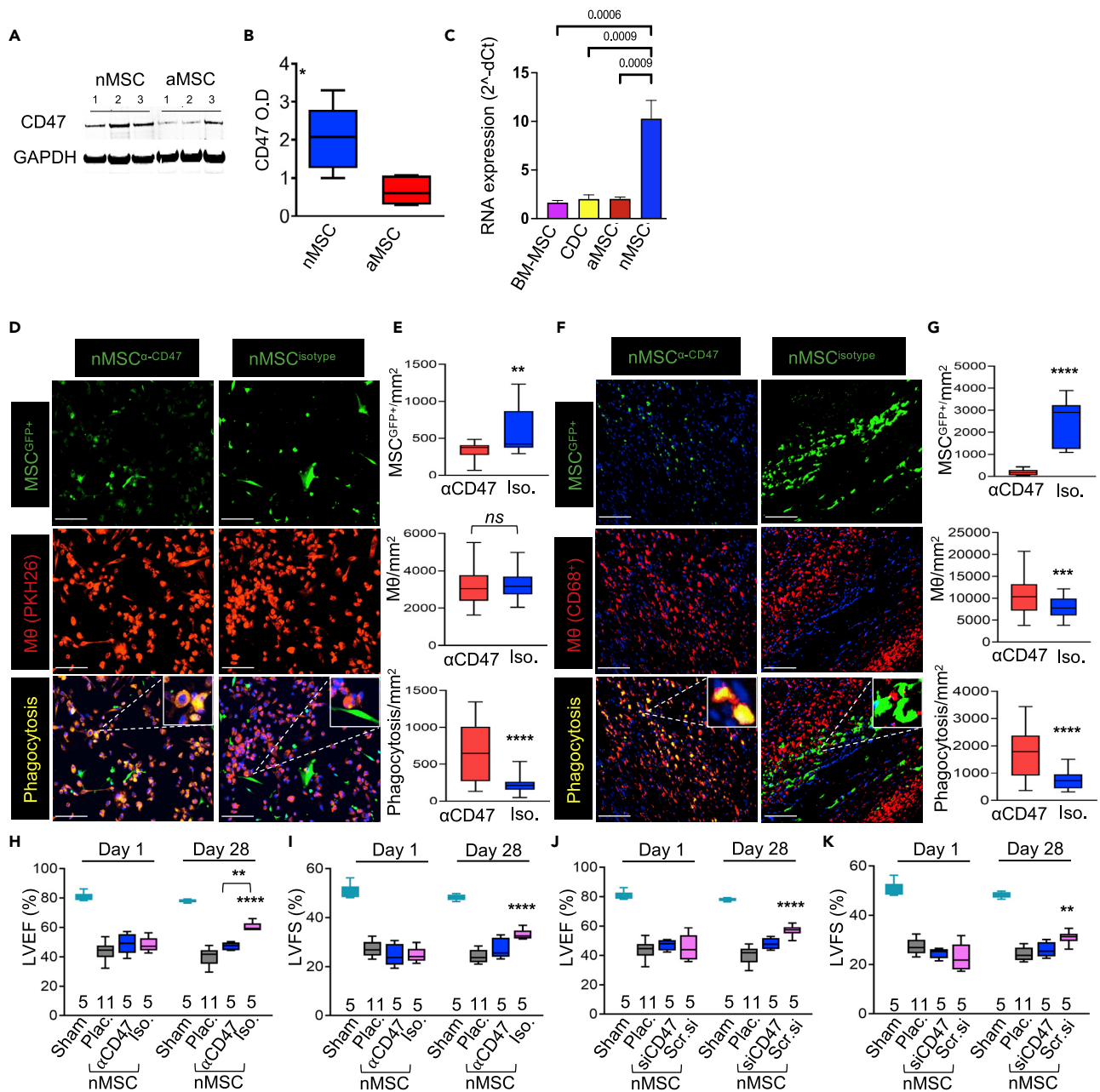
Figure 5. CD47 expression on nMSC inhibits phagocytosis

(A and B) Immunoblots showing expression of CD47 in nMSCs and aMSCs (N = 3) (A) and quantification (B).

(C) Comparative expression of miR-34a in BM-MSC, CDC, aMSCs and nMSCs.

(D) Representative images of *in vitro* phagocytosis assays of nMSCs$^{\alpha-CD47}$ and nMSCs$^{\alpha-isotype}$ (scale bars = 75 μm).

(E) Quantification of nMSCs$^{\alpha-isotype}$ (cell retention, green), Mφs (PKH26, red) and phagocytic cells (yellow) compared to nMSCs$^{\alpha-CD47}$.

(F) Representative images of nMSC$^{\alpha-CD47}$ and nMSC$^{\alpha-isotype}$ phagocytosis assays in rat MI model.

(G–I) (G) Quantification of nMSCs$^{\alpha-isotype}$ (cell retention, green), CD68$^+$ Mφ (red) and phagocytic cells (yellow) compared to nMSCs$^{\alpha-CD47}$ in the rat MI model (N = 4). The rat MI model transplanted with nMSCs$^{\alpha-CD47}$ showed reduced LVEF (H) and LVFS (I) compared with nMSCs$^{\alpha-isotype}$ (N = 5–11).

(J and K) (J) LVEF and LVFS (K) of rat hearts injected with nMSCs^{CD47siRNA} or nMSCs$^{scr.siRNA}$ in the rat MI model (N = 5–11).

Data were analyzed by Prism GraphPad^{Tm} software. Nonparametric Mann Whitney tests (E and G) and One-way ANOVA (H–K) were used for comparative analysis. Data were represented as mean ± SEM (*p < 0.05, **p < 0.01, ***p < 0.001 and ****p < 0.0001).
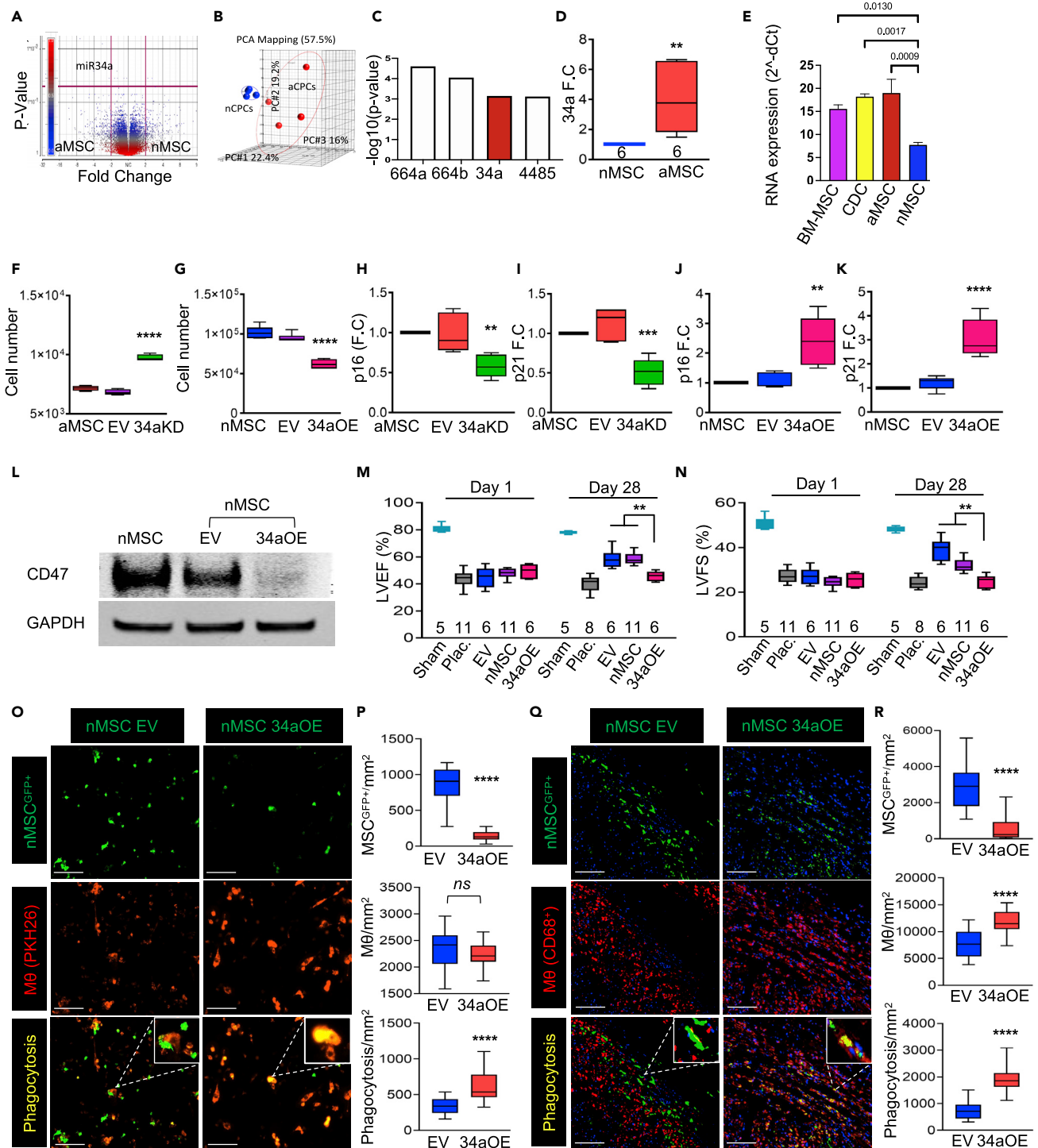
Figure 6. miR34a-regulated paracrine secretion and exosomes in MSCs

(A) Volcano plot showing differential expression of miRNAs in nMSCs and aMSCs.

(B) Principal Component Analysis (PCA) showing the distribution of different biological samples of nMSCs or aMSCs according to miRNA gene ontology of molecular function.

(C) Histograms showing the expression of miR-664a, −664b, −34a, and −4485 in aMSCs compared with nMSCs.

D) Quantitative expression of miR-34a in aMSC and nMSC.

(E) Comparative expression of miR-34a in BM-MSC, CDC, aMSCs and nMSCs (E), by RT-PCR (N = 6).

Figure 6. *Continued*

(F and G) Cell growth as measured by alamarBlue assays in aMSCs^{34aKD} and nMSCs^{34aOE}.

(H and I) Quantification of p16 (H) and p21 (I) in aMSCs^{34aKD} by RT-PCR (N = 5). (J and K) Quantification of p16 (J) and p21 (K) in nMSCs^{34aOE} by RT-PCR.

(L) CD47 expression in nMSCs following miR34a overexpression.

(M and N) LVEF (M) and LVFS (N) of rat hearts injected with nMSCs^{34aOE} compared with nMSCs transduced with empty vector (nMSCs^{EV}), nMSCs, and IMDM (vehicle control) (N = 5–11).

(O and P) (O) Representative images of *in vitro* phagocytosis assays of nMSCs^{34aOE} and nMSCs^{EV} (scale bars = 75 μm). nMSCs^{EV} (cell retention, green), Mφs (PKH26, red), and phagocytic cells (yellow) compared to nMSCs$^{miR34a\ OE}$ were quantified using ImageJ (P).

(Q) Representative images of *in vivo* phagocytosis assays in the rat MI model showing phagocytosis, CD68$^+$ cells, and retention of nMSCs^{34aOE} compared with nMSCs^{EV}.

(R) Quantification of actively proliferating nMSCs$^{\alpha\text{-isotype}}$ (cell retention, green), CD68$^+$ Mφ (red), and phagocytic cells (yellow) compared to nMSCs$^{\alpha-CD47}$ in rat myocardium (N = 4).

Data were analyzed by Prism GraphPad^{Tm} software. One-way ANOVA (C–L, N and O) test and nonparametric Mann Whitney test (Q and S) were used for comparative analysis. Data were represented as mean ± SEM (*p < 0.05, **p < 0.01, ***p < 0.001 and ****p < 0.0001).

aMSCs^{EV} at 28 days post-MI (Figures 6N and 6O). Furthermore, nMSCs$^{miR-34A-OE}$ co-cultured with M1 PKH26 macrophages demonstrated significantly increased phagocytosis compared with nMSCs^{EV} (Figures 6P and 6Q). Similarly, injection of nMSCs$^{miR-34A-OE}$ significantly increased phagocytosis in the rat MI myocardium compared with injection of nMSCs^{EV} (Figures 6R and 6S).

MicroRNA-34a regulates secretome production in MSCs

Independently secreted cytokines are key secretome components and, significantly, are present at higher levels in nMSCs than in aMSCs (Sharma et al., 2017). To further delineate whether miR-34a controls independently secreted cytokines in the secretome, we quantified seven key cardioprotective paracrine factors in the secretomes of aMSCs and nMSCs after knockdown and overexpression of miR-34a and transfection of the empty vehicle control. ELISA-based quantitative analysis of total conditioned media demonstrated that miR-34a knockdown resulted in significant increases in HGF, SCF, IGF, platelet-derived growth factor beta (PDGF-β), and FGF2 in the aMSC secretome (Figure 7A), but did not affect levels of VEGF-A and SDF1α. In contrast, overexpression of miR-34a in nMSCs significantly decreased the levels of all seven secreted paracrine factors (Figure 7B). Using computational analysis (TargetScan and Dianna Tools) to better understand these effects, we determined that the mRNA transcripts of PDGF, HGF, IGF-1, FGF2 and SCF have direct binding sites for miR-34a in their 3′ untranslated regions (UTRs) (Figure S11). miRNAs inhibit protein translation by binding directly to short sequence fragments in 3′ UTRs. To test whether miR-34a can directly target the mRNAs of these cardioprotective genes to mediate the observed decreases in expression, regions of the corresponding 3′UTRs were cloned downstream of firefly luciferase. In the presence of wild-type 3′UTR sequences, a significant reduction in luciferase activity was seen for the PDGF, HGF, IGF-1, FGF2, and SCF genes upon cotransfection with a miR-34a mimic (Figure 7C). Mutation of the miR-34a binding sites within the 3′UTR constructs blocked inhibition of luciferase expression by the miR-34a mimics, demonstrating that PDGF, HGF, IGF-1, FGF2, and SCF are miR34a targets (Figure 7C). As promotion of angiogenesis is one of the primary mechanisms of cardiac repair by these seven cardioprotective cytokines, we performed endothelial tube formation assays to determine if miR-34a–related changes in protein expression regulate this functional outcome. Knockdown of miR-34a in aMSCs (aMSCs^{-34aKD}) resulted in a significant increase in total endothelial tube length compared with vehicle alone and overexpression of miR34a in nMSCs (nMSCs^{34aOE}) (Figures 7D–7F). Similarly, in the MI model, injected nMSCs$^{miR-34A-OE}$ significantly reduced cardiac functional recovery (Figures 7N and 7O) and decreased formation of arterioles and neovessels as well as myocardial fibrosis at 28 days when compared with nMSCs^{EV} or nMSCs (Figures 7J–7L, 7O and 7P). Injected aMSCs$^{miR-34a-KD}$ significantly improved cardiac function (Figures 7N and 7O), augmented the preservation/formation of arterioles and neovessels, and resulted in smaller infarcted areas and reduced fibrosis when compared with injection of aMSCs or aMSCs^{EV} at 28 days post-MI (Figures 7G–7I, 7M, and 7N).

We previously showed that HSF1 not only activates key upstream regulators of cytokine production to modify secretome protein enrichment of nMSCs, but also increases production of exosomes in nMSCs compared with aMSCs (Sharma et al., 2017). However, the mechanism for these changes in the nMSC secretome was unknown. We hypothesized that miR-34a plays a key role in modifying exosome production by downregulating the expression of HSF1 and associated downstream cytokines as well as exosome levels. Indeed, we found increased levels of exosomes in aMSCs^{34aKD} and reduced exosome levels in nMSCs^{34aOE},
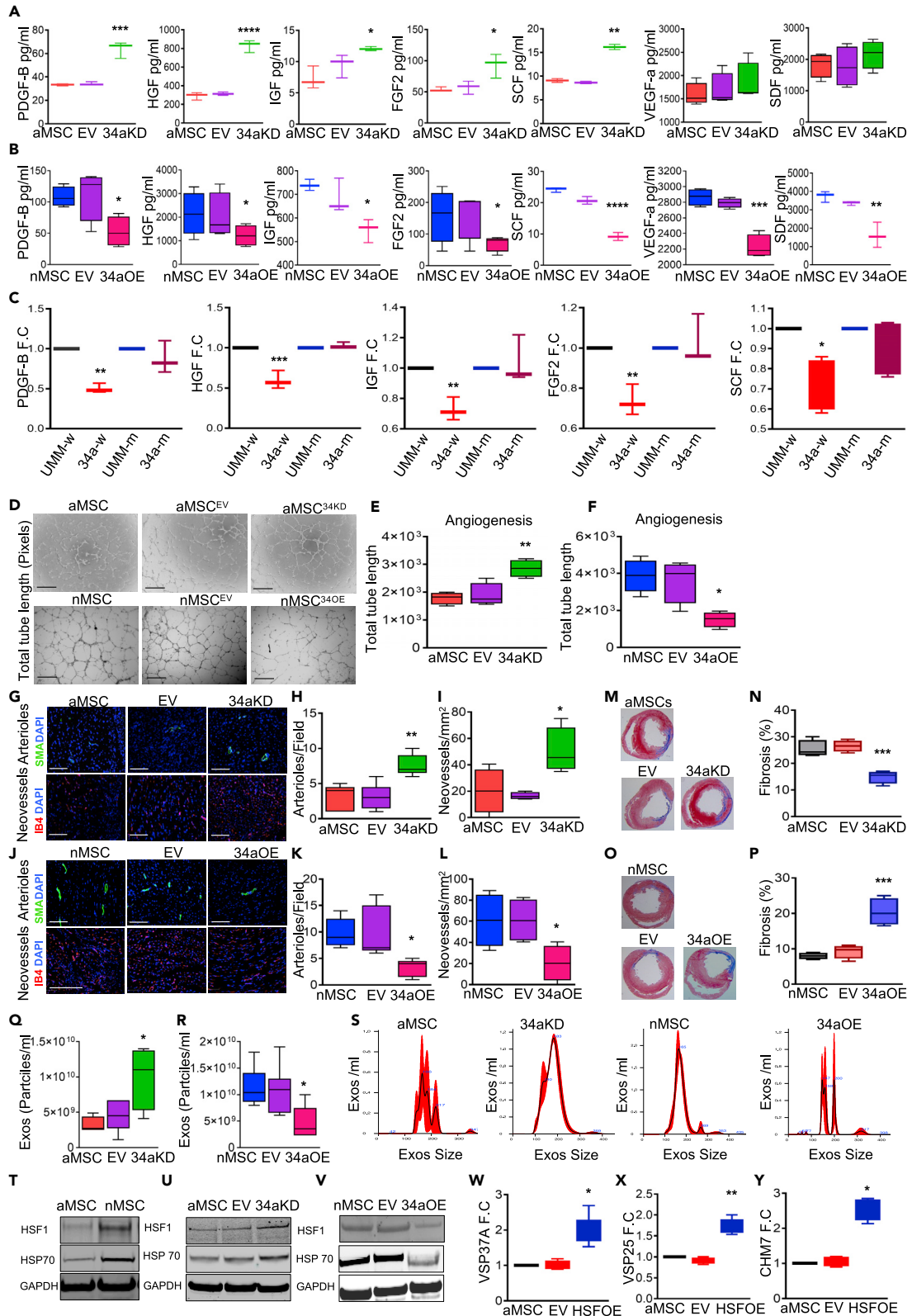
Figure 7. Effect of miR-34a on the MSCs secretome

(A and B) Quantification of seven cardioprotective paracrine factors from aMSC^{34aKD} (A) and nMSCs^{34aOE} (B) (N = 3–4).

(C) Luciferase reporter plasmids were constructed with either the wild-type miR-34a 3′UTR segment containing the miR-34a binding site with PDGFB, HGF, IGF1, FGF2, and SCF. Luciferase activity was normalized by the ratio of the firefly and Renilla luciferase signals (N = 3).

(D–F) Tube formation assay in aMSCs^{34aKD} and nMSCs^{34aOE} (D) and quantification (E and F) (N = 4).

(G–I) (G) Representative images of arterioles (α-smooth muscle actin [α-SMA]) and neovessel (IB4) formation in rat myocardium after transplantation of aMSCs^{34aKD}. Quantification of arterioles (H) and neovessel (I) formation (N = 4).

(J–L) (J) Representative images of arterioles (α-smooth muscle actin [α-SMA]) and neovessel (IB4) formation in rat myocardium after transplantationof nMSCs^{34aOE} . Quantification of arterioles (K) and neovessel (L) formation (N = 4).

(M–P) Representative images of fibrosis at POD 28 after aMSC^{34aKD} (M) and nMSC^{34aOE} transplantation in MI rat model (O) and quantification (N and P, respectively) (N = 6–8). Exosome concentration in total conditioned media (TCM) by NanoSight after gain and loss of miR-34a function in aMSCs (Q) and nMSCs (R) (N = 4–6).

(S) NanoSight tracking analysis of exosome particle number and size distribution analyzed in TCM isolated from aMSCs^{34aKD} and nMSCs^{34aOE}.

(T–V) Immunoblot analysis of HSF1 and HSP70 expression levels in aMSCs and nMSCs (T), HSP70 and HSF1 expression levels increased after aMSC^{34aKD} in aMSCs (U), and miR-34^{OE} in nMSCs (V).

(W–Y) Exosome biogenesis genes VSP37A (W), VSP25 (X), and CHM7 (Y) after HSF-1 overexpression (N = 4–6).

Data were analyzed by Prism GraphPad^{Tm} software. One-way ANOVA was used for comparative anlaysis. Data were represented as mean ± SEM (*p < 0.05, **p < 0.01, ***p < 0.001 and ****p < 0.0001).

as visualized by Nanosight (Figures 7Q–7S, Videos S1, S2, S3, and S4), and significant enrichment of HSF1 and HSP70 expression in nMSCs compared with aMSCs by immunoblot analysis (Figure 7T). To further analyze the miR-34a/HSF1 axis, we assessed aMSCs^{34aKD} and nMSCs^{34aOE} and showed HSP70 and HSF1 protein expression to be significantly higher after miR-34a knockdown in aMSCs and significantly lower after miR-34a overexpression in nMSCs (Figures 7U and 7V). To elucidate the mechanism by which miR-34a and HSF1 influence exosome production, miR-34a was overexpressed in aMSCs, and quantitative RT-PCR was performed for genes known to play a role in exosome biogenesis. We found that miR-34a overexpression in aMSCs failed to upregulate three candidate exosome biogenesis molecules: VSP37a, VSP25, and CHM7 (Figure S12). These proteins were upregulated by HSF1 overexpression in aMSCs, (Figures 7W–7Z). These results suggest that HSF1 (rather than miR-34a) regulates exosome biogenesis directly.

DISCUSSION

Many aspects of successful cardiac repair by transplanted cardiac stem cells can be greatly influenced by variables that depend on both the host response and the characteristics of the transplanted cells, including stem cell retention, secretome composition, and immunorejection (Sharma et al., 2017). Until now, transplanted cardiac stem cells and the host response to cellular therapy have been considered separately, as many studies have used immunocompromised or immunosuppressed animal models. A clinically relevant model must acknowledge that the ischemic myocardium during cellular therapy is a composite of the host, the transplanted cells, and their interactions. Herein, we took an integrated approach to identify the most effective cardiac cell type for repairing the ischemic myocardium in the setting of an immunocompetent host response to address the crucial question of how the secretome of the transplanted cardiac stem cells interacts with the immune cells present in the ischemic myocardium.

We evaluated the therapeutic potential of five clinically relevant cell types in immunocompromised animals (RNU rats) with MI. Nude rats were first used to assess therapeutic potential in isolation, because normal immunocompetent animals have varying levels of tolerance for different transplanted cell types. In a head-to-head comparison, we demonstrated that nMSCs outperformed all other clinically tested cell types in improving cardiac function in the rat MI model. We next provided several lines of evidence that, from a translational point of view in an immunocompetent MI rodent model, cardiac repair is optimized by robust cellular retention, which in turn directly modulates the host immune response through the secretome of the transplanted cells to restore cardiac function and alleviate left ventricular remodeling. The reductions in neutrophils and monocyte-derived circulating macrophages and the increases in Tregs and M2 macrophages in the ischemic myocardium indicates that transplanted nMSCs do not act in a linear pattern, but rather target multiple arms of the immune system. In addition, modulation of Tregs in the host myocardium established that the functional benefit of nMSC therapy is not because of an acute, inflammation-based, wound-healing response that rejuvenates the infarcted area of the heart (Vagnozzi et al., 2020).

Strikingly, using single-cell sequencing, we found that cell-defined characteristics determined by chronological aging may affect the efficacy of cellular therapy. nMSCs provided the greatest therapeutic benefit

when compared with adult-derived cells. This provided the opportunity to perform a direct comparison between these two cell types isolated with similar methodology. It has been well demonstrated that cardiac repair following ischemic injury is supported, at least in part, by immunomodulation and macrophage polarization (Dai et al., 2020; Galuppo et al., 2017; Shiraishi et al., 2016). In an immunocompetent model, we found that the superior functionality of nMSCs is because of their retention in the host myocardium and immunomodulation of neutrophils, macrophages, and T cells.

To mechanistically define nMSC retention in ischemic myocardium, we took a multipronged approach. First, we performed comparative deep RNA sequencing analysis of nMSCs and aMSCs and identified differentially-expressed mRNAs by single-cell mRNA sequencing using the 10 × Genomics platform. Differentially higher expression of CD47 in nMSCs and its enrichment in all 4 clusters belonging to nMSCs made it an attractive candidate for further analysis. CD47 is a transmembrane protein expressed on the surface of various solid, hematologic cancers and cancer stem cells. CD47 interacts with its ligand SIRPα on macrophages, resulting in inhibition of phagocytosis (16–29). The presence of CD47 on cardiomyocytes prevents their phagocytosis and the clearance of dead myocytes in the ischemic myocardium (Zhang et al., 2017). Herein, we highlight another antiphagocytic role of CD47 in cardiac repair, resulting in prolonged retention of transplanted nMSCs. Higher CD47 expression by nMSCs triggers a "don't eat me" signal. These data are particularly provocative as other stem/progenitor cells (e.g., induced pluripotent stem cells), need to express CD47 in order to create an immunosuppressive response (Deuse et al., 2019). The downstream antiphagocytic mechanism of CD47 action has been well-defined (Chao et al., 2012; Majeti et al., 2009; Willingham et al., 2012; Zhang et al., 2018). By computational analysis followed by experimental verification, we identified miR34a-5p, an age-related microRNA, as the master regulator of CD47.

We previously demonstrated that nMSCs have greater proliferative potential than adult MSCs. Additionally, compared with the aMSC secretome, the nMSC secretome contained more cardioprotective paracrine factors and exosomes, explaining their greater regenerative potential (Sharma et al., 2017). In our study, miR34a overexpression in nMSCs reduced both their proliferative potential and cardiac recovery after MI. In contrast, miR-34a knockdown in aMSCs increased their proliferative potential and significantly improved cardiac function with reduced fibrosis. These results establish the critical role of miR34a in determining the quality of secretome in particular and the functional activity of cell therapy as such.

We found that miR-34a overexpression resulted in decreased secretion of PDGF, HGF, IGF-1, FGF2, and SCF from nMSCs. In general, miRNAs regulate the transcription of target coding RNAs by binding to their 3'UTRs, inhibiting further translation and destabilizing the translational complex (Seo et al., 2017). We identified and verified the presence of direct miR-34a binding sites in the 3'UTR regions of the mRNAs encoding these paracrine factors, revealing another level at which the functional abilities of nMSCs can be controlled. We further found that overall exosome production varied inversely with miR-34a. We demonstrated previously that heat shock factor 1 (HSF1) regulated both protein secretion and exosome production (Sharma et al., 2017). Interestingly, overexpression of miR-34a resulted in decreased HSF1/HSP 70 expression, whereas knockdown of miR-34a led to increased HSF1/HSP70 expression. Thus, miR-34a likely potentiates exosome production by decreasing the expression of HSF1/HSP70 and other components of this pathway. These results indicate that a miR34a-HSF1-CD47 axis is critical for the ability of nMSCs to robustly improve cardiac function in the injured myocardium.

We found that nMSCs have an innate cardioprotective phenotype because of their optimal secretome production, which is tightly regulated by miR-34a for both independently secreted cytokines and exosomes. These results broaden our understanding of how cell therapy leads to cardiac repair. In addition, our results suggest that full, effective repair of the injured myocardium and the associated reversal of left ventricular dysfunction requires both cellular and biochemical characteristics such as CD47 expression and secretome composition. We demonstrated that miR-34a is a key molecule directly affecting cellular retention by targeting CD47 and cardioprotective cytokines. miR-34a, through HSF1, also affects exosome production. These results establish a direct correlation between a microRNA and secretome composition affecting the functional potential of a cell therapy. Interestingly, miR34a knockdown reversed the deficits of aged aMSCs to recover the functional activity of the ischemic myocardium. Thus, our study shows that cellular characteristics determined by chronological age have an adverse effect on the efficacy of cellular therapy and that the secretome is the functional unit of nMSCs.

Limitations of the study

A limitation of our study is that the *in vitro* conditions were different for each cell type because of their source of isolation and its diversity (Hare et al., 2012; Saha et al., 2019; Sharma et al., 2017). Unfortunately, it is not possible to culture and expand all the different cell populations under identical conditions. Although our study demonstrated that a single cell type (nMSCs) produced superior cardiac functional recovery compared to other cells types, a combinatorial approach using different cell types together might provide superior benefits to any one cell type by promoting multiple concurrent processes such as modulation of immunity, influencing remodeling, and favoring angiogenesis or other beneficial tissue responses (Lim et al., 2014). Transgenic knockouts of specific subpopulations of macrophages will be necessary to delineate their precise role(s) in cardiac functional recovery after nMSC injection in rats with MI (Vagnozzi et al., 2020). As such rat models are not currently available, we cannot definitively identify the macrophage population that mediates the beneficial effects of nMSCs. However, our study demonstrates that nMSC transplantation induces significantly higher levels of CD163$^+$ anti-inflammatory macrophages and reduces inflammatory CD68$^+$CCR2$^+$ and CD68$^+$CX3CR1$^+$ macrophages, confirming that nMSCs actively modulate the inflammatory response in the rat MI model. Our results confirm that CD47 expression in nMSCs helps these cells to evade phagocytic macrophages, thereby enhancing cardiac functional recovery after MI. However, other factors such as resistance to environmental stress, anti-apoptosis, increased cell adhesion molecules expression, and genes associated with cell cycle and proliferation may contribute to increased cell survival and retention in the infarcted myocardium *in vivo*.

Conclusions

Our data identify nMSCs as a potent cell type with translational potential and illuminate cellular mechanisms responsible for the beneficial effects of stem cell therapy. Together, our data strongly support the concept that nMSCs promote functional recovery of the heart via an active, immunomodulatory response that improves cell retention and promotes both exosome production and the secretion of independent cytokines. Given these mechanisms of action and the efficacy of nMSCs in the immunocompetent rat MI model, nMSCs are a promising new cell type that is uniquely positioned for successful translation to the clinic.

STAR★METHODS

Detailed methods are provided in the online version of this paper and include the following:

- KEY RESOURCES TABLE
- RESOURCE AVAILABILITY
  - Lead contact
  - Materials availability
  - Data and code availability
- EXPERIMENTAL MODELS AND SUBJECT DETAILS
  - Human tissue samples for nMSCs preparation
  - Animal studies
  - Flow cytometry analysis
  - Gating strategy for flow cytometry analysis
  - RNA extraction and RT-PCR analysis
  - μParaflo™ MicroRNA microarray assay
  - Single cell analysis
  - miRNA selection
  - Immunoblot analysis
  - AlamarBlue cell proliferation assays
  - Preparation of conditioned media and paracrine factor quantification
  - Angiogenesis assay
  - NanoSight particle analysis of exosomes
  - Cell transplantation and echocardiography
  - Myocardial histology
  - Myocardial viability
  - Lentivirus production and transduction
  - Luciferase assays
  - Preparation of dead nMSCs

- ○ Macrophage depletion
- ○ CD47 knockdown in nCPCs by siRNA
- ○ *In vitro* phagocytosis assays
- ○ *In vivo* phagocytosis assays
- ○ Pathway enrichment and upstream regulator analyses
- ● STATISTICAL ANALYSIS

SUPPLEMENTAL INFORMATION

Supplemental information can be found online at https://doi.org/10.1016/j.isci.2022.104656.

AUTHOR CONTRIBUTIONS

S.K., R.M., and M.G. conceived the study. R.M., M.G. S.S., L.D., W.C., L.C., P.S., X.F., A.J., J.H. A.S., G.B., M.A., D.M., A.T., and T.K. performed experiments and generated all the data shown in the manuscript. S.K., P.Y., R.B., and C. C. provided theoretical assessment of the project and advice in experimental design. S.K., R.M. S.S., D.L., M.E.D., R.B., J.M.H, and M.G. interpreted the data and wrote the manuscript.

DECLARATION OF INTEREST

The authors declare no competing interests.

REFERENCES

Alvey, C., and Discher, D.E. (2017). Engineering macrophages to eat cancer: from "marker of self" CD47 and phagocytosis to differentiation. J. Leukoc. Biol. *102*, 31–40. https://doi.org/10.1189/jlb.4ri1216-516r.

Bolstad, B.M., Irizarry, R.A., Astrand, M., and Speed, T.P. (2003). A comparison of normalization methods for high density oligonucleotide array data based on variance and bias. Bioinformatics *19*, 185–193. https://doi.org/10.1093/bioinformatics/19.2.185.

Chao, M.P., Weissman, I.L., and Majeti, R. (2012). The CD47–SIRPα pathway in cancer immune evasion and potential therapeutic implications. Curr. Opin. Immunol. *24*, 225–232. https://doi.org/10.1016/j.coi.2012.01.010.

Dai, Y., Wang, S., Chang, S., Ren, D., Shali, S., Li, C., Yang, H., Huang, Z., and Ge, J. (2020). M2 macrophage-derived exosomes carry microRNA-148a to alleviate myocardial ischemia/reperfusion injury via inhibiting TXNIP and the TLR4/NF-κB/NLRP3 inflammasome signaling pathway. J. Mol. Cell. Cardiol. *142*, 65–79. https://doi.org/10.1016/j.yjmcc.2020.02.007.

Deuse, T., Hu, X., Gravina, A., Wang, D., Tediashvili, G., De, C., Thayer, W.O., Wahl, A., Garcia, J.V., Reichenspurner, H., et al. (2019). Hypoimmunogenic derivatives of induced pluripotent stem cells evade immune rejection in fully immunocompetent allogeneic recipients. Nat. Biotechnol. *37*, 252–258. https://doi.org/10.1038/s41587-019-0016-3.

Duran, J.M., Makarewich, C.A., Sharp, T.E., Starosta, T., Zhu, F., Hoffman, N.E., Chiba, Y., Madesh, M., Berretta, R.M., Kubo, H., et al. (2013). Bone-derived stem cells repair the heart after myocardial infarction through transdifferentiation and paracrine signaling mechanisms. Circ. Res. *113*, 539–552. https://doi.org/10.1161/circresaha.113.301202.

Dyavar Shetty, R., Velu, V., Titanji, K., Bosinger, S.E., Freeman, G.J., Silvestri, G., and Amara, R.R. (2012). PD-1 blockade during chronic SIV infection reduces hyperimmune activation and microbial translocation in rhesus macaques. J. Clin. Invest. *122*, 1712–1716. https://doi.org/10.1172/jci60612.

Frangogiannis, N.G. (2012). Regulation of the inflammatory response in cardiac repair. Circ.

Res. *110*, 159–173. https://doi.org/10.1161/circresaha.111.243162.

Galuppo, P., Vettorazzi, S., Hövelmann, J., Scholz, C.J., Tuckermann, J.P., Bauersachs, J., and Fraccarollo, D. (2017). The glucocorticoid receptor in monocyte-derived macrophages is critical for cardiac infarct repair and remodeling. FASEB J. *31*, 5122–5132. https://doi.org/10.1096/fj.201700317r.

Gao, X., Gulari, E., and Zhou, X. (2004). In situ synthesis of oligonucleotide microarrays. Biopolymers *73*, 579–596. https://doi.org/10.1002/bip.20005.

Goto, H., Kojima, Y., Matsuda, K., Kariya, R., Taura, M., Kuwahara, K., Nagai, H., Katano, H., and Okada, S. (2014). Efficacy of anti-CD47 antibody-mediated phagocytosis with macrophages against primary effusion lymphoma. Eur. J. Cancer *50*, 1836–1846. https://doi.org/10.1016/j.ejca.2014.03.004.

Hare, J.M., Fishman, J.E., Gerstenblith, G., DiFede Velazquez, D.L., Zambrano, J.P., Suncion, V.Y., Tracy, M., Ghersin, E., Johnston, P.V., Brinker, J.A., et al. (2012). Comparison of allogeneic vs autologous bone marrow–derived mesenchymal stem cells delivered by transendocardial injection in patients with ischemic cardiomyopathy: the POSEIDON randomized trial. JAMA *308*, 2369–2379. https://doi.org/10.1001/jama.2012.25321.

Ito, T., Ishigami, M., Matsushita, Y., Hirata, M., Matsubara, K., Ishikawa, T., Hibi, H., Ueda, M., Hirooka, Y., Goto, H., et al. (2017). Secreted ectodomain of SIGLEC-9 and MCP-1 synergistically improve acute liver failure in rats by altering macrophage polarity. Sci. Rep. *7*, 44043. https://doi.org/10.1038/srep44043.

Jaiswal, S., Jamieson, C.H., Pang, W.W., Park, C.Y., Chao, M.P., Majeti, R., Traver, D., van Rooijen, N., and Weissman, I.L. (2009). CD47 is upregulated on circulating hematopoietic stem cells and leukemia cells to avoid phagocytosis. Cell *138*, 271–285. https://doi.org/10.1016/j.cell.2009.05.046.

Kamerkar, S., LeBleu, V.S., Sugimoto, H., Yang, S., Ruivo, C.F., Melo, S.A., Lee, J.J., and Kalluri, R. (2017). Exosomes facilitate therapeutic targeting of oncogenic KRAS in pancreatic cancer. Nature *546*, 498–503. https://doi.org/10.1038/nature22341.

Kaur, R., Sloan, L.A., Blanchard, A.D., Smith, J.L., Churcher, I., Wayne, G.J., and Ludbrook, S.B. (2013). A phenotypic screening approach in cord blood-derived mast cells to identify anti-inflammatory compounds. J. Biomol. Screen *18*, 1223–1233. https://doi.org/10.1177/1087057113500073.

Konstandin, M.H., Toko, H., Gastelum, G.M., Quijada, P., De La Torre, A., Quintana, M., Collins, B., Din, S., Avitabile, D., Völkers, M., et al. (2013). Fibronectin is essential for reparative cardiac progenitor cell response after myocardial infarction. Circ. Res. *113*, 115–125. https://doi.org/10.1161/circresaha.113.301152.

Lim, J.Y., Park, M.J., Im, K.I., Kim, N., Jeon, E.J., Kim, E.J., Cho, M.L., and Cho, S.G. (2014). Combination cell therapy using mesenchymal stem cells and regulatory T-cells provides a synergistic immunomodulatory effect associated with reciprocal regulation of TH1/TH2 and th17/treg cells in a murine acute graft-versus-host disease model. Cell Transplant. *23*, 703–714. https://doi.org/10.3727/096368913x664577.

Lun, A.T., Bach, K., and Marioni, J.C. (2016). Pooling across cells to normalize single-cell RNA sequencing data with many zero counts. Genome Biol. *17*, 75. https://doi.org/10.1186/s13059-016-0947-7.

Majeti, R., Chao, M.P., Alizadeh, A.A., Pang, W.W., Jaiswal, S., Gibbs, K.D., Jr., van Rooijen, N., and Weissman, I.L. (2009). CD47 is an adverse prognostic factor and therapeutic antibody target on human acute myeloid leukemia stem cells. Cell *138*, 286–299. https://doi.org/10.1016/j.cell.2009.05.045.

Métayer, L.E., Vilalta, A., Burke, G.A.A., and Brown, G.C. (2017). Anti-CD47 antibodies induce phagocytosis of live, malignant B cells by macrophages via the Fc domain, resulting in cell death by phagoptosis. Oncotarget *8*, 60892–60903. https://doi.org/10.18632/oncotarget.18492.

Mishra, R., Vijayan, K., Colletti, E.J., Harrington, D.A., Matthiesen, T.S., Simpson, D., Goh, S.K., Walker, B.L., Almeida-Porada, G., Wang, D., et al. (2011). Characterization and functionality of cardiac progenitor cells in congenital heart patients. Circulation *123*, 364–373. https://doi.org/10.1161/circulationaha.110.971622.

Nahrendorf, M., Pittet, M.J., and Swirski, F.K. (2010). Monocytes: protagonists of infarct inflammation and repair after myocardial infarction. Circulation *121*, 2437–2445. https://doi.org/10.1161/circulationaha.109.916346.

Polański, K., Young, M.D., Miao, Z., Meyer, K.B., Teichmann, S.A., and Park, J.E. (2020). BBKNN: fast batch alignment of single cell transcriptomes. Bioinformatics *36*, 964–965. https://doi.org/10.1093/bioinformatics/btz625.

Rieckmann, M., Delgobo, M., Gaal, C., Büchner, L., Steinau, P., Reshef, D., Gil-Cruz, C., Horst, E.N.T., Kircher, M., Reiter, T., et al. (2019). Myocardial infarction triggers cardioprotective antigen-specific T helper cell responses. J. Clin. Invest. *129*, 4922–4936. https://doi.org/10.1172/jci123859.

Saha, P., Sharma, S., Korutla, L., Datla, S.R., Shoja-Taheri, F., Mishra, R., Bigham, G.E., Sarkar, M., Morales, D., Bittle, G., et al. (2019). Circulating exosomes derived from transplanted progenitor cells aid the functional recovery of ischemic myocardium. Sci. Transl. Med. *11*, eaau1168. https://doi.org/10.1126/scitranslmed.aau1168.

Segers, V.F.M., and Lee, R.T. (2008). Stem-cell therapy for cardiac disease. Nature *451*, 937–942. https://doi.org/10.1038/nature06800.

Seo, H.H., Lee, S.Y., Lee, C.Y., Kim, R., Kim, P., Oh, S., Lee, H., Lee, M.Y., Kim, J., Kim, L.K., et al. (2017). Exogenous miRNA-146a enhances the therapeutic efficacy of human mesenchymal stem cells by increasing vascular endothelial growth factor secretion in the ischemia/reperfusion-injured heart. J. Vasc. Res. *54*, 100–108. https://doi.org/10.1159/000461596.

Sharma, S., Mishra, R., Bigham, G.E., Wehman, B., Khan, M.M., Xu, H., Saha, P., Goo, Y.A., Datla, S.R., Chen, L., et al. (2017). A deep proteome analysis identifies the complete secretome as the functional unit of human cardiac progenitor cells. Circ. Res. *120*, 816–834. https://doi.org/10.1161/circresaha.116.309782.

Shiraishi, M., Shintani, Y., Ishida, H., Saba, R., Yamaguchi, A., Adachi, H., Yashiro, K., and Suzuki, K. (2016). Alternatively activated macrophages determine repair of the infarcted adult murine heart. J. Clin. Invest. *126*, 2151–2166. https://doi.org/10.1172/jci85782.

Simpson, D.L., Mishra, R., Sharma, S., Goh, S.K., Deshmukh, S., and Kaushal, S. (2012). A strong regenerative ability of cardiac stem cells derived from neonatal hearts. Circulation *126*, S46–S53. https://doi.org/10.1161/circulationaha.111.084699.

Telukuntla, K.S., Suncion, V.Y., Schulman, I.H., and Hare, J.M. (2013). The advancing field of cell-based therapy: insights and lessons from clinical trials. J. Am. Heart Assoc. *2*, e000338. https://doi.org/10.1161/jaha.113.000338.

Tseng, D., Volkmer, J.P., Willingham, S.B., Contreras-Trujillo, H., Fathman, J.W., Fernhoff, N.B., Seita, J., Inlay, M.A., Weiskopf, K., Miyanishi, M., et al. (2013). Anti-CD47 antibody-mediated phagocytosis of cancer by macrophages primes an effective antitumor T-cell response. Proc. Natl. Acad. Sci. USA *110*, 11103–11108. https://doi.org/10.1073/pnas.1305569110.

Vagnozzi, R.J., Maillet, M., Sargent, M.A., Khalil, H., Johansen, A.K.Z., Schwanekamp, J.A., York, A.J., Huang, V., Nahrendorf, M., Sadayappan, S., et al. (2020). An acute immune response underlies the benefit of cardiac stem cell therapy. Nature *577*, 405–409. https://doi.org/10.1038/s41586-019-1802-2.

Vasandan, A.B., Jahnavi, S., Shashank, C., Prasad, P., Kumar, A., and Prasanna, S.J. (2016). Human Mesenchymal stem cells program macrophage plasticity by altering their metabolic status via a PGE2-dependent mechanism. Sci. Rep. *6*, 38308. https://doi.org/10.1038/srep38308.

Wehman, B., and Kaushal, S. (2015). The emergence of stem cell therapy for patients with congenital heart disease. Circ. Res. *116*, 566–569. https://doi.org/10.1161/circresaha.115.305821.

Wernli, G., Hasan, W., Bhattacherjee, A., van Rooijen, N., and Smith, P.G. (2009). Macrophage depletion suppresses sympathetic hyperinnervation following myocardial infarction. Basic Res. Cardiol. *104*, 681–693. https://doi.org/10.1007/s00395-009-0033-3.

Willingham, S.B., Volkmer, J.P., Gentles, A.J., Sahoo, D., Dalerba, P., Mitra, S.S., Wang, J., Contreras-Trujillo, H., Martin, R., Cohen, J.D., et al. (2012). The CD47-signal regulatory protein alpha (SIRPa) interaction is a therapeutic target for human solid tumors. Proc. Natl. Acad. Sci. USA *109*, 6662–6667. https://doi.org/10.1073/pnas.1121623109.

Wolf, F.A., Angerer, P., and Theis, F.J. (2018). SCANPY: large-scale single-cell gene expression data analysis. Genome Biol. *19*, 15. https://doi.org/10.1186/s13059-017-1382-0.

Wolock, S.L., Lopez, R., and Klein, A.M. (2019). Scrublet: computational identification of cell doublets in single-cell transcriptomic data. Cell

Syst. *8*, 281–291.e9. https://doi.org/10.1016/j.cels.2018.11.005.

Xu, Q., Seeger, F.H., Castillo, J., Iekushi, K., Boon, R.A., Farcas, R., Manavski, Y., Li, Y.G., Assmus, B., Zeiher, A.M., et al. (2012). Micro-RNA-34a contributes to the impaired function of bone marrow-derived mononuclear cells from patients with cardiovascular disease. J. Am. Coll. Cardiol. *59*, 2107–2117. https://doi.org/10.1016/j.jacc.2012.02.033.

Zhang, M., Hutter, G., Kahn, S.A., Azad, T.D., Gholamin, S., Xu, C.Y., Liu, J., Achrol, A.S., Richard, C., Sommerkamp, P., et al. (2016). Anti-CD47 treatment stimulates phagocytosis of glioblastoma by M1 and M2 polarized

macrophages and promotes M1 polarized macrophages in vivo. PLoS One *11*, e0153550. https://doi.org/10.1371/journal.pone.0153550.

Zhang, S., Yeap, X.Y., DeBerge, M., Naresh, N.K., Wang, K., Jiang, Z., Wilcox, J.E., White, S.M., Morrow, J.P., Burridge, P.W., et al. (2017). Acute CD47 blockade during ischemic myocardial reperfusion enhances phagocytosis-associated cardiac repair. JACC Basic Transl. Sci. *2*, 386–397. https://doi.org/10.1016/j.jacbts.2017.03.013.

Zhang, X., Chen, W., Fan, J., Wang, S., Xian, Z., Luan, J., Li, Y., Wang, Y., Nan, Y., Luo, M., et al. (2018). Disrupting CD47-SIRPα axis alone or combined with autophagy depletion for the

therapy of glioblastoma. Carcinogenesis *39*, 689–699. https://doi.org/10.1093/carcin/bgy041.

Zheng, G.X.Y., Terry, J.M., Belgrader, P., Ryvkin, P., Bent, Z.W., Wilson, R., Ziraldo, S.B., Wheeler, T.D., McDermott, G.P., Zhu, J., et al. (2017). Massively parallel digital transcriptional profiling of single cells. Nat. Commun. *8*, 14049. https://doi.org/10.1038/ncomms14049.

Zhou, Y., Zhou, B., Pache, L., Chang, M., Khodabakhshi, A.H., Tanaseichuk, O., Benner, C., and Chanda, S.K. (2019). Metascape provides a biologist-oriented resource for the analysis of systems-level datasets. Nat. Commun. *10*, 1523. https://doi.org/10.1038/s41467-019-09234-6.

STAR★METHODS

KEY RESOURCES TABLE

Antibodies		
RESOURCE	IDENTIFIER	SOURCE
Antibodies for flow cytometry		
C-kit	561,443	BD, APC
CD90	559,869	BD, APC
CD105	561,443	BD, PE
CD45	561,443	BD, PE
CD34	sc-7045	SCBT, Goat pAb
CD31	561,443	BD, FITC
CD3	557,030	BD, APC
CD4	561,578	BD, PE-Cy7
CD8	561,614	BD, V450
CD25	17-0390-82	eBioscience, APC
FoxP3	320,008	Biolegend, PE
CD45	202,205	Biolegend, FITC
CD68	MCA341A488	BioRad, FITC
CD163	NBP2-39099	Novus, AF647
CD11c	11-0114-82	Invitrogen, FITC
CD11b/c	562,222	BD, PE-Cy7
MHCII	17-0920-82	BD, APC
RP1	550,002	BD, PE
CD16/CD32	553,142	BD, Fc Block
Antibody for IHC		
IB4	121,413	Invitrogen, AF 594
SMA	F3777	Sigma, FITC
CD68	ab31630	Abcam, Mouse pAb
CD163	ab199427	Abcam, Rabbit pAb
CCR2	ab273050	Abcam, Rabbit pAb
CX3R1	ab8021	Abcam, Rabbit pAb
Antibody for *in vitro* and *in vivo* phagocytosis		
CD47	BE0283	Bio X Cell, Mouse mAb
Isotype Control	BP0297	Bio X Cell, IgG1 Ab
GFP	MAB3580	Millipore, Mouse mAb
Antibody for immunoblot		
CD47	ab108415	Abcam, Rabbit mAb
HSF1	4356s	CST, Rabbit mAb
HSP70	610,607	BD, Mouse mAb
GAPDH	MAB374	Millipore, Mouse mAb
CD68	ab31630	Abcam, Mouse pAb
CD31	ab24590	Abcam, Mouse pAb
MHC-II	ab55152	Abcam, Mouse pAb
LAMP-2	ab203224	Abcam, Rabbit pAb
TSG101	612,697	BD, Mouse mAb

Continued		
RESOURCE	IDENTIFIER	SOURCE
RAB27A	ab108983	Abcam, Rabbit mAb
Reagents		
DAPI	F6057	Sigma
Calcein, AM	C1430	Thermofisher Sci.

RESOURCE AVAILABILITY

Lead contact

The raw data, analytic methods, and study materials will be publicly available as online-only Data Supplement. Study materials will be provided after a reasonable request. Inquiries can be directed to the lead contact, Dr. Sunjay Kaushal.

Materials availability

This study did not generate new unique reagents.

Data and code availability

- No sequence data was generated
- No code data was generated
- Any additional information required to reanalyze the data reported in this paper is available from the lead contact on request.

EXPERIMENTAL MODELS AND SUBJECT DETAILS

Human tissue samples for nMSCs preparation

This study was approved by the Institutional Review Board and the Institutional Animal Care and Use Committee at the University of Maryland School of Medicine. After parental or patient consent was given, specimens from the right atrial appendage were obtained from neonatal (n = 25; 30 $\pm$ 20 mg) and adult patients (n = 43; 100 $\pm$ 30 mg) during routine cardiac surgeries. All adults were undergoing coronary artery bypass grafting. From our cell bank, we randomly chose 7 neonatal mesenchymal stromal cell lines from neonates having normal functioning myocardium (collected during operations for structural abnormalities) and 7 adult mesenchymal stromal cell lines from male patients with normal functioning myocardium for all experimental studies.

Animal studies

This study was approved by Institutional Animal Care and Use Committee at the University of Maryland School of Medicine. Both male and female rats were used for *in vivo* experiments.

Generation of neonatal and adult mesenchymal stromal cells, cardiosphere-derived cells, umbilical cord blood cells, and bone marrow–derived mesenchymal stem cells.

Cardiac neonatal and adult mesenchymal stromal cells were isolated from right atrial appendage samples (Sharma et al., 2017). Human cardiosphere-derived cells were generated using a modified version of the protocol (Mishra et al., 2011; Simpson et al., 2012). Human cord blood mononuclear cells (Kaur et al., 2013) (Stem Cell Technologies #70007.1) and bone marrow–derived mesenchymal stem cells (BM-MSCs) for *in vivo* experiments were cultured as described previously (Hare et al., 2012). We randomly selected 3-7 different biological patient-derived stem cell lines for all experimental studies.

Flow cytometry analysis

Heart tissue was harvested at day 5 post-MI from all the treated animals and was minced and digested by Collagenase D (Roche) at 37 °C for 50 minutes at rocking platform (180–200 rpm). After enzymatic digestion cells suspension was filtered through a 70-μm cell strainer (Fisher Scientific #22363548) and centrifuged at 500 g for 10 min, to lyse the red blood cells, cells pellet was incubated in ACK lysing buffer (Gibco

A10492-01) at room temperature for 3–5 mins and cells were washed with FACS washing buffer (2.5% FBS in PBS without calcium and magnesium). Cells were re-suspended in washing buffer and samples were incubated with Fc-Block (anti-rat CD16/CD32, 0.5 μg per 1 million cells) before incubation with isotype controls or primary antibodies according to manufacturer's instructions. Cells were then washed with washing buffer and approximately 2×10^5 events (cells) were analyzed by flow cytometry (LSR-Fortessa) and populations gated as detailed below and sorted by FlowJo software. key resources table shows description of antibodies, including manufacture and antibody specificity.

Gating strategy for flow cytometry analysis

T cells and T-regulator cells, cells were first gated (FSC-A vs. SSC-A) as lymphocytes. For Total T cells, the lymphocyte gate is further analyzed for CD3 and CD8, For T-regulatory cells CD4 cells were gated and from this gate CD25$^+$ and Fox-P3$^+$ double positive cells were determined. For macrophages, neutrophils, and dendritic cells, CD45 cells were gated. CD45 positive cells were further analyzed for CD68 for macrophage, CD45$^+$/CD11b$^+$/RP1$^+$ (Neutrophils) and CD11c$^+$/MHC-11$^+$ as dendritic cells.

RNA extraction and RT-PCR analysis

Total RNA was isolated from cells using miRNeasy kits from Qiagen and real-time PCR, according to the manufacturer's instructions. A cDNA synthesis kit (Applied Biosystems, CA) was used to reverse transcribe 500 ng RNA/reaction according to the manufacturer's protocol. We used 5 ng cDNA for each sample in 20-μL PCR reactions. Each reaction was performed in triplicate using an ABI Fast SYBR-Green reaction mix. Quantitect primer assays for each primer set were obtained from Qiagen; probes were purchased from Thermofisher Inc. (Waltham, MA). Cycle threshold (CT) values of the housekeeping gene were subtracted from the corresponding gene of interest. The fold change of expression level for each gene was determined by the expression 2^-dCT. Final values were averaged, and results were represented as fold expression with the standard error of the mean (SEM).

μParaflo™ MicroRNA microarray assay

Microarray assays were performed using a service provider (LC Sciences, Inc). Four to 8 μg of total RNA samples were 3'-extended with a poly(A) tail using poly(A) polymerase. RNA was amplified using a novel signal amplification strategy by labeling samples with an affinity tag for signal amplification after hybridization. As the signal intensity increases from 1 to 65,535, the corresponding color changes from blue to green, to yellow, and to red. An oligonucleotide tag was then ligated to the poly(A) tail for later fluorescent dye staining. Hybridization was performed overnight on a μParaflo microfluidic chip using a micro-circulation pump (Atactic Technologies) (Gao et al., 2004). On the microfluidic chip, each detection probe consisted of a chemically modified nucleotide coding segment complementary to a target microRNA (from miRBase, http://mirbase.org) or other RNA (control or customer defined sequences) and a spacer segment of polyethylene glycol to extend the coding segment away from the substrate. The detection probes were made by *in situ* synthesis using PGR (photogenerated reagent) chemistry. The hybridization melting temperatures were balanced by chemical modifications of the detection probes. Hybridization used 100 μL 6xSSPE buffer (0.90 M NaCl, 60 mM Na$_2$HPO$_4$, 6 mM EDTA, pH 6.8) containing 25% formamide at 34 °C. After RNA hybridization, a tag conjugated to Cy3 dye was circulated through the microfluidic chip for dye staining. Fluorescence images were collected using a laser scanner (GenePix 4000B, Molecular Device) and digitized using Array-Pro image analysis software (Media Cybernetics). Data were analyzed by first subtracting the background and then normalizing the signals using a LOWESS filter (Locally weighted Regression) using miRBase Release 20.0 (Bolstad et al., 2003). Signal p-values are provided and a signal with p-value <0.01 is detectable.

Single cell analysis

Cardiac tissue was collected from three neonate and three adult patients and the respective nMSCs and aMSCs were separated using magnetic bead sorting and sequenced using 10x Chromium technology with Single Cell 3' v2 chemistry. The reads were aligned to the GRCh38 human reference genome using the Cell Ranger analysis pipeline (10x Genomics Cell Ranger 2.1.0) (Zheng et al., 2017). Raw counts were fed into the Scanpy single cell analysis library in Python(Wolf et al., 2018). Doublets were filtered using the Scrublet method and the dataset was filtered to remove cells with less than 1500 total transcripts or 780 distinctly expressed genes (Wolock et al., 2019). The dataset was also filtered to remove cells with a greater than 20% mitochondrial gene fraction. The dataset was further reduced to only include genes

that were expressed in at least 20 cells. Each batch was normalized using the SCRAN cell pooling methodology and utilized a coarse Leiden clustering to identify initial cell pools (Lun et al., 2016). Jurkat cells that were initially spiked into the samples for quality control purposes during sequencing were filtered from the dataset using CD3E and CD3D gene expression to identify cells with normalized expression greater than 1. The batch balanced k-nearest neighbors batch correction algorithm was applied in conjunction with a ridge regression to align the individual batches and remove sources of unwanted technical variance (Polański et al., 2020). The batch corrected data was clustered using the Leiden algorithm at a resolution of 0.5. The differential gene expression was computed on the clusters using non-batch corrected data using the rank_genes_groups function in Scanpy with the default t-test method. The top 100 upregulated genes were fed into the Metascape pathway analysis tool (Zhou et al., 2019). The final dataset contained 61,979 cells, 60.5% of which were aMSCs and 39.5% were nMSCs.

miRNA selection

Significantly differential expressed miRs (False detection rate (FDR<1.0%, $p < 0.05$, fold change more than 1.5)) between nMSC and aMSC were identified by miRNA microarray analysis. Our screen identified miR34a-5p as highly and differentially expressed in aMSCs.

Immunoblot analysis

Cells were lysed with radioimmunoprecipitation assay buffer (RIPA) (Cell Signaling Technology, Boston, MA # 9806) containing complete protease and phosphatase inhibitor cocktail (Roche Applied Science, Indianapolis, IN #11836170001). Cell lysates were prepared, and protein concentrations were determined using the bicinchoninic assay (BCA) method (ThermoFisher Scientific, Waltham, MA #23209). SDS-PAGE (4–12% gels) (Invitrogen #NP0335BOX) were used to resolve 40 μg of protein lysate. Proteins were transferred to PVDF membranes (Bio-rad #1620177) using semidry or wet transfer methods and probed with specific antibodies to. We analyzed 5 biological replicates for immunoblot analysis. The Odyssey system from Li-Cor Biosciences was used for detection and quantitative analysis.

AlamarBlue cell proliferation assays

Cell proliferation was assessed using alamarBlue (10% of the total volume of the medium), as per the manufacturer's instructions. Briefly, 5,000 cells/well were seeded in 96-well plates in their respective media. After overnight incubation at 37 °C, 10 μL of alamarBlue Cell Viability Reagent (Invitrogen cat #1933424, Carlsbad, CA) was added per well and absorbance was measured immediately (basal absorbance) and after 3 h incubation at 37 °C (proliferation absorbance). To obtain the actual absorbance, the basal absorbance was subtracted from the proliferation absorbance.

Preparation of conditioned media and paracrine factor quantification

Following miR34a manipulation, aMSCs and nMSCs were grown in complete media until they reached 85%–90% confluence ($\sim$1 × 10^6 cells). The cells were washed with warm Ham's F12 medium twice and changed to fresh Ham's F12 basal medium. Conditioning of the cells was continued for 72 h to obtain secretome/total conditioned medium (TCM). Secretome was precleared of cellular debris and particulate matter by centrifugation at 4,000 × g for 30 min, followed by 10,000 × g for 30 min to remove microvesicles (Millipore Inc, Billerica, MA #UFC900324). Total protein content was quantified using the BCA method. To normalize the protein content we used the following formula: (concentration factor) × (total volume of medium)/(total protein content of conditioned medium).[8] The protein contents of the conditioned media were quantified using the BCA method and normalized to a total of 1 mg protein. ELISA was performed for human VEGFA, SDF-1, PDGFB, IGF-1, ANG-1, FGF2, SCF, and HGF in the core facility at the University of Maryland School of Medicine using human-specific ELISA kits (Millipore and R&D systems Inc. Billerica, MA), according to the manufacturer's protocol.

Angiogenesis assay

The formation of tube-like structures was assessed in a Matrigel-coated 24-well plate (BD Biosciences, San Jose, CA) (Sharma et al., 2017). Briefly, human umbilical vein cells (HUVEC-1, ATCC PCS-100-010TM) were counted and seeded at a density of 20,000 cells/mm^2 on reduced growth factor–containing Matrigel BD Biosciences, San Jose, CA #354230) with the addition of endothelial manipulation in aMSCs and nMSCs or conditioned medium from Empty a control. Cells were imaged after 6–12 h and a complete image of

each well was reconstructed. The total tube length was then measured using ImageJ64, NIH (http://rsb.info.nih.gov/ij).

NanoSight particle analysis of exosomes

Exosomes from nMSCs and aMSCs after miR-34a overexpression and knockdown were isolated and analyzed. Briefly, exosomes were purified from total conditioned medium (TCM) by size exclusion chromatography using a Sepharose 2B column (Sigma-Aldrich #CL2B300) and eluted fractions were analyzed using a NanoSight NS300 (405-nm laser diode) for the presence of vesicles 40–120-nm in diameter.

Cell transplantation and echocardiography

MI was induced by permanent ligation of the left anterior descending (LAD) coronary artery in immunodeficient (RNU rats, Charles River)/immunocompetent rats (Brown Norway, Charles River) (weight: 160–220 g). Briefly, heart was exposed via a left thoracotomy, and the proximal LAD was ligated. One million cells were suspended in 100 μL vehicle (IMDM-base media without any essential nutrients or growth factors) and injected into the myocardium at 4 sites adjacent to the infarct while IMDM serves as placebo control. Baseline echocardiograms were acquired 1 day after procedure (post-operative echocardiographic examinations at 24 h to insure similar extend of induction of MI), 7 days and at 28 days post- MI. Two-dimensional and M-mode echocardiography was performed using the VisualSonics Vevo 2100 ultrasound unit (VisualSonics, Toronto, Canada) to assess metrics of left ventricular size and function. Images were obtained from the parasternal long axis and the parasternal short axis at the midpapillary level.

Myocardial histology

Rat hearts were excised under anesthesia after collection of echocardiographic data and perfused with 10% formalin solution, (Sigma Aldrich #HT501128). Tissues were cryopreserved using 30% sucrose (prepared in 1xPBS) and embedded in OCT (Fisher Scientific, TissueTek #NC1029572). Sections were cut to 7 μm using a commercial cryostat and stained for different antibodies according to manufacturer's instruction. Cells and tissue sections were counterstained with 4′,6-diamidino-2-phenylindole (DAPI) nuclear stain (Sigma #F6057).

Myocardial viability

The midline technique for infarct size determination was used (Sharma et al., 2017). Briefly, the infarct size was calculated using Masson's trichrome-stained sections at various levels along the long axis. The stained sections were analyzed by ImagePro software. To calculate the viable and nonviable tissue, the number of red pixels (viable tissue) and blue pixels (nonviable tissue) were measured and the ratio of nonviable tissue/overall number of pixels was calculated. Six sections per animal and at least 5-8 animals per group were analyzed.

Lentivirus production and transduction

Manipulation of gene expression was performed by lentiviral transduction. All lentiviruses were produced in HEK293T. HEK293T cells (American Type Culture Collection, Manassas, VA) were cultured in DMEM media (CellGro) supplemented with 10% fetal bovine serum (Thermofisher Scientific #A38402-02). Lentivectors were co-transfected with the VSV-G envelope–expressing plasmid pMD2.G (gift from Didier Trono, Addgene plasmid #12259) and packaging plasmid psPAX2 (gift of Didier Trono, Addgene plasmid #12260) and concentrated using PEG-it (System Biosciences). The titer of each lentivirus preparation was calculated based upon the amount of virus required to yield 50% GFP+ cells following transduction of 100,000 MSCs. Cells were transduced in 12-well dishes with increasing amounts of lentivirus in media supplemented with 8 μg/mL polybrene (Sigma Aldrich #TR-1003). Three days after transduction, the percentage of GFP + cells in each well were determined by flow cytometry using Accuri C6 (Becton Dickinson). The amount of virus necessary to obtain 50% GFP + cells was set to MOI = 0.5. Subsequent cell transductions were performed at MOI = 2 (~90% GFP + cells at day 3 days post-transduction) for analysis of MSC phenotypes and function. In each experiment, transduction efficiency was confirmed by flow cytometric determination of the percentage of GFP+ cell populations.

Luciferase assays

All luciferase assays were conducted using the miRGlo vector (Promega #E1330), which co-expresses firefly and Renilla luciferase. HEK293T cells (ATCCn CRL-3216) were transfected with Lipofectamine 2000

(ThermoFisher Scientific #11668030). All experimental samples were transfected with miR-Glo–based lucif-erase reporters and the miR34a versus miR550b miR mimic (Dharmacon). Two days post-transfection, cells were harvested in passive lysis buffer and luciferase values were quantified using a dual luciferase reporter assay kit (Promega #E1910) according to the manufacturer's instructions on a Perkin Elmer Victor X3 Multi-label Reader. For each condition, 3 independent wells were transfected per experimental replicate. Firefly luciferase in each well was normalized to Renilla luciferase values from same well. The entire experiment was repeated at least 3 times.

Preparation of dead nMSCs

nMSCs (1 million cells/100 μL) were frozen at −80 °C and thawed at 55°C for 10 min. This freeze-thaw cycle was repeated a total of 3 times to prepare dead MSCs. Cell debris was resuspended in 100 μL IMDM. Lipo-polysaccharide (LPS, 10 μg/100 μL, Sigma #L2630) was injected as a positive control to induce an immune response following LAD ligation. The activation and the increased $CD68^+$ macrophage following LPS injec-tion was measured in the explanted in infarcted hearts by immunohistochemistry.

Macrophage depletion

To determine whether macrophages are important for nMSC-mediated MI recovery, macrophages in rats were depleted using clodronate liposomes as described (Ito et al., 2017; Vagnozzi et al., 2020; Wernli et al., 2009). Briefly, Brown-Norway rats were intraperitoneally injected with clodronate liposomes (Encapsula Nano Sciences # CLD-8901) and Encapsome (control liposomes prepared in PBS) were intraperitoneally (1 mL/100 g body weight) on pre-MI and post MI days 1 and 5 on Brown Norway rats. One million nMSCs cells with and without clodronate liposomes were injected. Macrophage depletion on day 5 was deter-mined by measuring $CD68^+$ macrophages by immunohistochemistry in the explanted hearts.

CD47 knockdown in nCPCs by siRNA

Knockdown of CD47 protein expression in nMSCs was performed using CD47 siRNA (Thermofisher Scien-tific, Inc #145977). Briefly, nMSCs were transfected with 100 nM siRNA at 60% confluency using Lipofect-amine RNAiMAX (Thermofisher Scientific, #13778030). The transfected cells were incubated in a humidified incubator at 37°C and 5% CO_2. Following 72 h of transfection, cells were harvested and CD47 knockdown efficiency was verified by immunoblot analysis.

In vitro phagocytosis assays

In vitro phagocytosis assays were performed using GFP^+ MSCs prepared using the lentiviral transduction system. Briefly, the monocyte cell line THP-1 (ATCC® # TIB-202) was differentiated to Mφ using 200 ng/mL phorbol 12-myristate 13-acetate (PMA, Sigma #P1585) and activated to Mφ1 (inflammatory phenotype) using LPS (100 ng/mL) (LPS, Sigma #L2630). Red-stained Mφ1s (PKH26, Red, Sigma #PKH26GL) and GFP-expressing aMSCs or nMSCs were co-cultured in RPMI complete medium for 24 h in 8-well chamber plates. To determine if CD47 blockade induces phagocytosis, $nMSCs^{GFP+}$ were incubated with anti-CD47 (Bio X Cell #BE0283) or control isotype antibodies (Bio X Cell #BP0297). The CD47 expression in nMSCs were blocked using anti-CD47 antibodies (Goto et al., 2014; Tseng et al., 2013; Zhang et al., 2016). Briefly, nMSCs (1 million cells/100μL) were incubated with anti-CD47 (1 μg/100 μL) and isotype control antibody for 1 h at 4 °C in HulaMixer Sample Mixer (ThermoFisher Scientific #15920D) Thereafter, cells were centrifuged at 1000 rpm for 5 min and unbound residual CD47 antibody in the supernatant was discarded. The antibody bound nMSC cell pellet was resuspended in 100 μL of IMDM for *in vitro* and *in vivo* phagocytosis. Similarly, to determine whether miR-34a overexpression inhibits CD47 expression and induces phagocytosis, nMSC were transduced with either the lentiviral vector overexpressing miR-34a (GFP^+) or the empty vector ex-pressing lentivirus as a control. The CD47 inhibition by miR-34a over expression in nMSC was validated by immunoblot. Phagocytic cells (yellow) and proliferating MSCs (green) were enumerated using an EVOS microscope. GFP^+ MSCs, Mφ, and phagocytic cells were enumerated using ImageJ. The experiment was repeated at least 3 times to obtain consistent results.

In vivo phagocytosis assays

In vivo phagocytosis assays were performed by transplanting 1 million $aMSC^{GFP+}$, $nMSC^{GFP+}$, anti-CD47 $nMSC^{GFP+}$, isotype antibody $nMSC^{GFP+}$, miR34a $^{GFP+}$ overexpressing nMSC, and vector control $^{GFP+}$ nMSC in rat MI model. Rats hearts collected after 48 h were sectioned and stained for GFP^+, $CD68^+$ cells by immunohistochemistry using specific antibodies. Images were acquired using an EVOS

microscope and cell retention analyzed by GFP expression, inflammation by CD68$^+$ cells, and phagocytic cells were analyzed for GFP$^+$ cells present within the CD68$^+$ cells (yellow color), respectively. Transplanted cell retention, CD68$^+$ cells, and phagocytic cells were enumerated using ImageJ. The experiment was repeated in at least 4 rats to observe consistent results for comparative analysis.

Pathway enrichment and upstream regulator analyses

Ingenuity Pathway Analysis (IPA) software (Qiagen Inc, USA) was used to perform pathway enrichment and upstream regulator analyses. A list of differentially expressed genes in a dataset with a minimum of 1.5-fold change and p < 0.05 significance when compared between the 2 groups was loaded into IPA. To identify biological pathways that were significantly regulated (p < 0.05; >0.05 ratio of differentially regulated genes involved in a pathway with the number of genes associated with the pathway), core analysis was performed on uploaded datasets based on fold change and *p* value significance in a dataset according to a standard protocol (Dyavar Shetty et al., 2012). We performed upstream regulator analysis to identify secretory factors, signaling mediators, and transcription factors that may not be differentially expressed at the transcriptional level but are predicted to be altered or modified (e.g., phosphorylation, acetylation, methylation) at the protein level, which may result in significant (p < 0.05 and > $\pm$ 2.0 *Z* score) activation or inhibition.

STATISTICAL ANALYSIS

Immunohistochemical analysis for GFP$^+$, CD68$^+$ and phagocytic cells *in vivo* were derived from 30 microscopic fields per tissue sample for each rat. Immunohistochemical data are representative for 4-5 rats in each cohort. Data are presented as Box-Whiskers plot representing median $\pm$ SD. *p < 0.05, **p < 0.01, ***p < 0.001, ****p < 0.0001, and 2-way ANOVA followed by Bonferroni's multiple comparisons test (ejection fraction, fractional shortening), one-way ANOVA followed by Tukey's multiple comparisons tests (fibrosis, immune cell analysis), Unpaired t test (flow cytometric analysis). Prism software from Graphpad Inc was used for data analyses. Comparative analysis of the cohorts was performed by t test followed by Mann Whitney test (phagocytosis assay, miRNA expression) or more than 2 cohorts were compared by one way ANOVA followed by Tukey's multiple comparisons test (paracrine analysis, angiogenesis, exosomes analysis). A p value less than 0.05 indicated statistical significance.